

Exact Coherent Structures with Broken Symmetry in Plane Couette Flow

---

A Thesis  
Presented to  
The Division of Mathematics and Natural Sciences  
Reed College

---

In Partial Fulfillment  
of the Requirements for the Degree  
Bachelor of Arts

---

Varchas Gopalaswamy

April 28, 2015



Approved for the Division  
(Physics)

---

Daniel Borrero



# Acknowledgements

Some people are of the opinion that acknowledgements ought not to consist of several pages of sappy sentiment. They are wrong.

---

Varchas Gopalaswamy

This thesis wouldn't have existed without my thesis advisor, Daniel Borrero. Thank you, Daniel, for suggesting an awesome thesis topic, for motivating me, for spending a ton of time correcting more terrible thesis drafts than any human should have to, for introducing me to dynamical systems theory, and for all the grad school help. Good luck with that Taylor-Couette system.

I would also like to thank John Gibson from the University of New Hampshire for making this thesis even remotely feasible by writing `Channelflow`, and for taking the time to correspond with me via email and Hangout. Your advice has been invaluable.

By definition, this thesis wouldn't have existed were I not a physics major, so I'd like to thank the department as a whole for being the greatest department at Reed. Thank you, Lucas, for being an extremely supportive academic advisor and for a challenging junior year. Thank you, Joel, for introducing me to the world of scientific computation, for running physics softball, and for your help with this thesis. Thank you, Darrell, for reminding me why quantum mechanics is awesome. Thank you, Johnny, for all the help with the grad school process. Thanks also to the physics seniors – shoutout to Julia and Neal for their tenure as the Pub Czars, Taras for his tenure as the Cookie Czar, Dan for putting up with the frantic late night calls for help, and Newton for being a rad office buddy. I will be proud to say that I was once a part of this group. You guys have made my time here special.



# Table of Contents

<b>Introduction</b> . . . . .	<b>1</b>
Plane Couette Flow . . . . .	1
Tackling Turbulence . . . . .	3
<b>Chapter 1: Equations of Flow</b> . . . . .	<b>11</b>
1.1 Formalisms . . . . .	11
1.1.1 The Eulerian Formulation . . . . .	12
1.1.2 The Fluid Particle . . . . .	12
1.2 Mass Conservation . . . . .	13
1.3 Conservation of Linear Momentum . . . . .	14
1.3.1 Stress . . . . .	14
1.3.2 Strain . . . . .	14
1.3.3 Surface Forces . . . . .	15
1.3.4 Newton's Second Law . . . . .	15
1.4 Plane Couette Flow . . . . .	16
<b>Chapter 2: Symmetry in plane Couette flow</b> . . . . .	<b>19</b>
2.1 Unbounded Navier-Stokes . . . . .	21
2.2 Plane Couette Flow . . . . .	21
2.3 Properties and Isotropy Subgroups of $\Sigma$ . . . . .	22
<b>Chapter 3: Numerics and Workflow</b> . . . . .	<b>27</b>
3.1 The Spectral Method . . . . .	27
3.1.1 The Residual . . . . .	27
3.1.2 Basis Functions . . . . .	29
3.1.3 Spatio-Temporal Discretization . . . . .	30
3.2 Newton-Krylov-Hookstep Method . . . . .	31
3.2.1 Newton's Method . . . . .	31
3.2.2 The Generalized Minimum Residual Method . . . . .	32
3.2.3 The Hookstep . . . . .	36
3.3 Recurrence Diagrams . . . . .	37
3.4 Parametric Continuation . . . . .	40
<b>Chapter 4: Results</b> . . . . .	<b>43</b>
4.1 The Gang of Four . . . . .	43

4.1.1	Visualizations . . . . .	44
4.2	Spanwise Continuation . . . . .	49
4.2.1	Linear Stability Analysis . . . . .	51
4.2.2	Return of the State Space . . . . .	53
4.3	Dissipation and Energy Input . . . . .	54
4.3.1	A New Projection . . . . .	54
4.3.2	The Search for Bifurcations, Part II . . . . .	57
<b>Conclusion</b>	. . . . .	<b>65</b>
<b>References</b>	. . . . .	<b>67</b>

# List of Figures

- |   |  |   |
|---|--|---|
| 1 | Streamlines on two surfaces of differing smoothness showcase the difference between laminar and turbulent flows. (a) In turbulent flow across an extremely smooth surface, streamlines break up into chaotic eddies and swirls, while in (b), the laminar flow across a rough surface preserves the streamlines. Reproduced from K.S. Choi, "Fluid Dynamics: The rough with the smooth", <i>Nature</i> , vol. 440, no, 7085, pp. 754-754, 2006 [1].  | 2 |
| 2 | A schematic of the plane Couette geometry. The upper and lower plates (white) extend infinitely in the plane, as does the fluid (blue) filling the gap between them. The upper and lower plates move with some constant velocity, and apply shear stresses to the fluid, resulting in fluid motion. While in general the plates can move in any direction, there is always a reference frame in which the plates move with equal but opposite velocity and it is convenient to work in this reference frame. According to convention, the $x$ axis is aligned along the plate velocity and is referred to as the <b>streamwise</b> direction. The $y$ -axis is aligned perpendicular to the plates and is referred to as the <b>wall-normal</b> direction. The $z$ -axis is normal to both axes and is referred to as the <b>spanwise</b> direction. | 2 |
| 3 | A cross-sectional representation of plane Couette flow, with the linear, laminar velocity profile shown. By symmetry, the laminar profile must be the same everywhere. At the top and bottom, where the fluid meets the walls, no-slip boundary conditions require that the wall-tangent velocity equal the boundary velocity.   | 3 |
| 4 | At each point in the fluid volume, the velocity field has a value that is described by three numbers, thus requiring three dimensions to track over time.  | 4 |
| 5 | A plot of a trajectory for the Lorenz system. The Lorenz system is an excellent example of a system in which the dynamics collapse onto an inertial manifold - in this case, the dynamics exist on a manifold of fractal dimension 2.06 [2], even though the state space is in three dimensions.   | 5 |

6	The four main categories of exact coherent structures. In all diagrams, only a particular flow structure is displayed, to demonstrate the various types of exact coherent structures. These could be, for example, iso-surfaces of velocity or energy. (a) An equilibrium solution, where the fluid structure does not change over time. (b) A relative equilibrium or traveling wave solution, where the state does not change in its own reference frame, but is translated relative to the observer. (c) A periodic orbit, where the flow state changes over time, but returns to the original state after some period $T$ . (d) A relative periodic orbit, where the flow state is periodic in its own reference frame, but is translated relative to the observer. . . . .	6
7	A schematic of a turbulent trajectory in state space and the coherent structures that guide it. (a) A turbulent trajectory in black appears chaotic and unpredictable in isolation. (b) When the underlying coherent structures in red are superimposed, however, the guiding of the dynamics by the exact coherent structures becomes evident. Starting from the left, the trajectory is pulled in towards an equilibrium (filled circle) along its stable manifold (arrow pointing inwards), before being ejected along its unstable manifold (arrow pointing outwards). The trajectory then shadows three periodic orbits, whose stable and unstable manifolds are not trivial to represent visually, but nonetheless exist, before being attracted and ejected by the final equilibrium and continuing on its way. Reproduced from D. Borrero-Echeverry, <i>Subcritical Transition to Turbulence in Taylor-Couette Flow</i> , PhD. Dissertation, Dept. of Physics, Georgia Institute of Technology, 2014 [3]. . . . .	7
8	The roll-streak structure of the Nagata upper branch equilibrium [4]. The in-plane velocity vectors in the periodic cell are displayed for the box walls, as well as the mid-plane. The coloration reflects the streamwise velocity, where blue indicates a large streamwise velocity out of the page, and red represents a large streamwise velocity into the page. The vortex that forms the roll is clearly visible on the near box wall, as is the streak running through the midplane of the box. These structural features are often seen in real turbulent flows, and solutions that approach the vicinity of this solution in the state space will take on some of this roll-streak structure. . . . .	8
2.1	A 2D pointwise inversion operation on two sets of vectors according to (2.6). . . . .	21
2.2	If the flow state is fixed by $\tau(\frac{1}{4}L_x, 0)$ , then the solution will have four repeating streamwise subcells, and it becomes more efficient to solely consider the subcell. . . . .	23

2.3 A simple demonstration that shifts and reflections do not commute in general. a) An object with a dashed outline is translated to the right, and then reflected across the vertical. b) The same object is reflected before it is translated to the right. Notice that the final positions of the object are not the same. . . . .	25
2.4 When periodic boundary conditions are imposed and translations are restricted to half-period lengths, shifts and reflects commute. a) An object is shifted and then reflected across the vertical. b) The same object is reflected across the vertical and then shifted. The final positions are the same, even if the intermediaries are not. . . . .	25
3.1 A demonstration of Newton's method in 1D on a simple function with the root at $x_r \approx 8.98$ . Starting at $x_0 = 13$ , the first tangent (black) has a zero at $x_1 \approx 10.5$ , the second tangent (red) has a zero at $x_2 \approx 9.4$ , and the third tangent (green) has a zero at $x_3 \approx 8.99$ . The method converges to within approximately $10^{-4}$ in just three steps. . . . .	32
3.2 If we assume the linear model remains valid for the entire step, we can sometimes be led astray. Because the function is linear only in the vicinity of the initial guess, the Newton step takes us very far away from the actual root we are trying to find, and will likely never converge. 33	
3.3 A recurrence plot which was used to find one of the new periodic orbits (P60) presented in this thesis. At each point, the value of $\mathfrak{R}(t, T) = \ \mathbf{u}(t+T) - \mathbf{u}(t)\ $ is plotted. Light colorations correspond to low values, and vice versa. Notice the long, thin streak of low values from $t = 200$ to $t = 450$ for $T \approx 60$ . A guess sourced from this band was the initial guess that led to the discovery of P60. . . . .	38

3.4 A flow chart that lays out the procedure used to find exact coherent structures. We begin by selecting a random initial state for the trajectory. This initial state can either be found by generating a truly random state, or by applying a small, random perturbation to known exact coherent structures. The desired symmetry constraints are then enforced, and the trajectory is integrated from  $t = 0$  to  $t = t'$ . After every time step, if the state's norm has dropped below some threshold  $R$  (I use 0.1), we assume that the trajectory has relaminarized, and find a new initial condition to work with. Once the integration is over, we generate the recurrence diagram according to (3.49), for some  $T_{\max}$ , and attempt to find any patterns that we would associate with exact coherent structures. If no patterns are found, we find another initial state and repeat the process. If there are some candidate patterns, we calculate the minimum  $\Re$  of that feature. If it is below about  $10^{-4}$ , we accept it as a potential solution, and pass it to the NKH solver. If  $\Re$  is not low enough, it is likely not a sufficiently good guess to cause the NKH solver to converge in a reasonable time, so we zoom in on the pattern and calculate a refined recurrence graph, until either the minimum value of the pattern is low enough, or it becomes apparent that the pattern is unlikely to produce a meaningful initial guess . . .

39

3.5 A schematic of a 1D bifurcation, that shows the variation of a solution  $x^*$  such that  $f(x^*) = 0$  as a function of a control parameter  $r$ . While the control parameter  $r < 2$ , there is only one, stable solution, on the left. At a critical value  $r = 2$ , however, a new solution emerges at  $x^* = -1$  in a **saddle-node bifurcation**. While  $2 < r < 4$ , the saddle-node splits into two, producing a stable lower solution (solid), and an unstable upper solution (dashed). As  $r$  approaches 4, the original stable solution and the new unstable solution approach each other until at  $r = 4$ , they annihilate in another saddle node bifurcation, leaving only the new stable solution. In higher dimensions, bifurcations can be incredibly complex, but we can nevertheless observe bifurcations of this form. . . . .

41

4.1 OP of P85. P85 is a fully symmetric orbit with period 85.50 in the HKW cell at  $Re = 400$ . Note the extreme symmetry of the prominent streaks visible in the mid-plane. The velocity field pictured here is the turbulent perturbation only; the laminar flow has been subtracted away. Available at <https://youtu.be/r6ac1b54vDk> . . . . .

45

4.2 OP of P60. P60 is another fully symmetric orbit with period 60.86 in the HKW cell with  $Re = 400$ . While it displays an ellipsoid streak structure similar to P85, the energy of these streaks is lower. The velocity field pictured here is the turbulent perturbation only; the laminar flow has been subtracted away. Available at <https://www.youtube.com/watch?v=ulyMrSfxW5U> . . . . .

4.3 OP of P32. P32 is a streamwise asymmetric periodic orbit fixed by the symmetry group  $S_z$ , which is functionally a mirror symmetry about the streamwise axis. However, notice that while P32 does not *exactly* maintain rotational symmetry about the streamwise axis, it bears remarkable similarity to P85 and P60. The rotational symmetry residual was  $10^{-3}$ , which is a few orders of magnitude lower than symmetries that are obviously not satisfied, but is not low enough ( $10^{-6}$ ) to be accepted as a legitimate symmetry. In the HKW cell at  $Re = 400$ , the period is 32.00, and the streamwise relative velocity is  $-0.5$  cell lengths per period. The velocity field pictured here is the turbulent perturbation only; the laminar flow has been subtracted away. Available at <https://www.youtube.com/watch?v=qDGbxX50bKY> . . . . .

47

4.4 OP of P8. P8 is a spanwise asymmetric periodic orbit fixed by the symmetry group  $S_x$ , which is functionally a rotation by  $\pi$  about the spanwise axis. In the HKW cell at  $Re = 400$ , the period is 8.32, and the spanwise relative velocity is  $2.29 \times 10^{-7}$  cell lengths per period. This number may seem low, but if it is not accounted for, the NKH solver cannot converge. P8 also has a rather short period, almost an order of magnitude shorter than most orbits recorded in the database at [channelflow.org](http://channelflow.org). Since the Arnoldi iteration has a time cost that scales linearly with the period, P8 has been the least computationally demanding period orbit to analyze. The velocity field pictured here is the turbulent perturbation only; the laminar flow has been subtracted away. Available at <https://youtu.be/-ad0U55T39w> . . . . .

48

4.5 2D state space projection of the Gang of Four and some reference equilibria. The basis vectors for the projection were constructed by orthonormalizing the initial states of each of the periodic orbits. This results in a 4D state space projection, of which we can take 2D slices (of which there are 6), or 3D slices (of which there are 4). The equilibria are fully symmetric, and were found by Halcrow [5]. Notice that the P8 orbit is separated by the equilibria from P85, P60 and P32, a feature that holds true in the other 5 2D projections. . . . .

49

4.6 Period as a function of spanwise cell length for P8. The data can be sectioned into three distinct parts. First, the **upper branch** (blue circles), which is the path that the continuation algorithm initially follows in parameter space. Second, the **transition branch** (green diamonds), which occurs after the **first turning point** (red, dashed circle). Third, the **lower branch** (orange rectangles), after the **second turning point** (purple, solid circle). Within the marked rectangular region, multiple distinct solutions exist for the same cell length, hinting at a bifurcation. Searches with higher resolution have pinned down the turning points to the interval  $L_z \in [2.8087, 2.8096]$  for the first turning point, and  $L_z \in [2.6150, 2.6157]$  for the second turning point. . . . .

50

4.7 Phase portrait of the Van Der Pol oscillator and its Hopf bifurcation, with trajectories in white. (a), for negative values of the bifurcation parameter, the single periodic orbit is unstable, so an initial condition that begins near the orbit spirals away from it. (b), when the bifurcation parameter is zero, there is no periodic orbit. (c), for positive values of the bifurcation parameter, the periodic orbit is stable, and initial conditions are attracted into the orbit. . . . .	51
4.8 All 20 unstable eigenvalues, and the 80 largest stable or marginal ( $ \lambda  << 1$ ) eigenvalues of P8, in the HKW cell at $Re = 400$ . Note that the eigenvalues come in conjugate pairs. Since there are eigenvalues with positive real parts, the periodic orbit is unstable, as expected. Note that since the Jacobian likely has full rank, and likely also has no repeating nonzero eigenvalues, there are several orders of magnitude more stable eigenvalues than there are unstable. Since the Arnoldi iteration will find the larger eigenvalues first, all the unstable eigenvalues are shown, whereas only the weakly stable eigenvalues are calculated.	52
4.9 Eigenvalues of P8 as a function of $L_z$ at the first turning point. When the real part of the eigenvalue switches sign, the associated eigenvector switches stability. Therefore, the line of eigenvalues with imaginary part $\approx \pm 0.3$ are of special interest. The real part of the eigenvalue likely switches sign at some $L_z \in [2.81509, 2.81857]$ , compared to the first turning point, which likely occurs for $L_z \in [2.8087205, 2.8096095]$	53
4.10 Eigenvalues of P8 as a function of $L_z$ at the second turning point. Here, two sets of eigenvalues have real parts that switch signs, first in the interval $L_z \in [2.96122, 2.96137]$ and second in the interval $L_z \in [2.96142, 2.9615]$ . The second stability switch is consistent with the position of the second turning point, which occurs in the interval $L_z \in [2.6150, 2.6157]$ . . . . .	54
4.11 The trajectory of a slight perturbation along the most unstable eigenvector, projected onto a difference slice of the same basis as in Figure 4.5. Notice that it keeps the general shape of the orbit that spawned it, at least for short time spans. . . . .	55
4.12 Poincar section of Figure 4.11, defined by the surface $e_2 = 0.26$ . Notice that the trajectory along the Poincar section spirals outwards, as we would expect for an unstable manifold with a complex eigenvalue. . .	55
4.13 Dissipation versus energy input for the Gang of Four. While the lesser members of the Gang remain clustered towards a input/dissipation of 2, P8 stays at a dissipation/input of 4. Due to P8's low period, the fine details of its orbit cannot be discerned here. The separation observed in Figure 4.5 is clearly reflected in this physically important projection.	56





# Introduction

I am an old man now, and when I die and go to heaven, there are two matters on which I hope for enlightenment. One is quantum electrodynamics, and the other is the turbulent motion of fluids. And about the former, I am optimistic.

---

Horace Lamb, 1932

Although much work has been done in understanding turbulence since Lamb's time, the twin problems of understanding the nature of the transition to turbulence and predicting the fine structure of turbulent flows remain unsolved to this day, having vexed scientists and engineers in much the same way a plucky band of Gauls did for Caesar. Understanding turbulence is vitally important, since turbulent flows appear in man-made scenarios such as the flow around ships or aircraft, as well as in natural scenarios like the atmosphere of Jupiter and the flow of blood in the heart. The degree to which a flow is turbulent is characterized by its **Reynolds number**  $Re$ , a dimensionless parameter that encodes the relative importance of inertial and viscous forces. At small  $Re$ , the **viscosity** of a fluid (which is analogous to fluid friction) dominates, and smooths out velocity gradients in the flow, resulting in well-ordered, **laminar** flow. At large  $Re$ , kinetic energy is dissipated at a lower rate, allowing for the existence of increasingly complex flow structures such as eddies or vortices (Figure 1). These structures, which are typical of **turbulence**, display large spatiotemporal variations and structure at a variety of spatial and temporal scales.

## Plane Couette Flow

Since viscosity is a dissipative force, a viscous fluid that has no energy input will eventually come to rest as its kinetic energy is dissipated into thermal energy. Therefore, sustaining turbulence requires continuous energy input. In the case of the flow between two infinite parallel plates (Figure 2), which known as plane Couette flow and is the focus of this thesis, this is provided by the wall shear. The geometry of the plane Couette system is extremely simple, with a geometrical parameter  $h$ , the half-distance between the parallel plates, and a kinematic parameter  $V$ , the constant

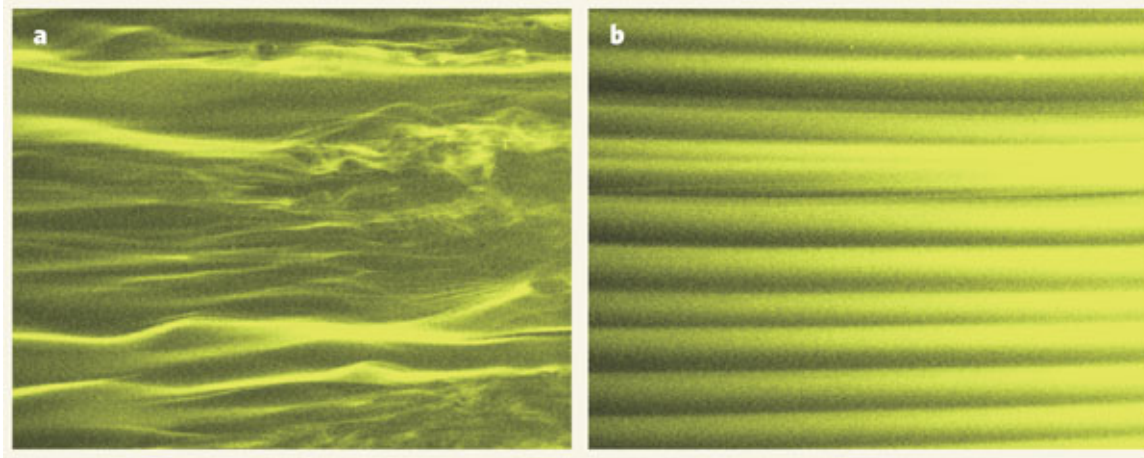


Figure 1: Streamlines on two surfaces of differing smoothness showcase the difference between laminar and turbulent flows. (a) In turbulent flow across an extremely smooth surface, streamlines break up into chaotic eddies and swirls, while in (b), the laminar flow across a rough surface preserves the streamlines. Reproduced from K.S. Choi, “Fluid Dynamics: The rough with the smooth”, *Nature*, vol. 440, no, 7085, pp. 754-754, 2006 [1].

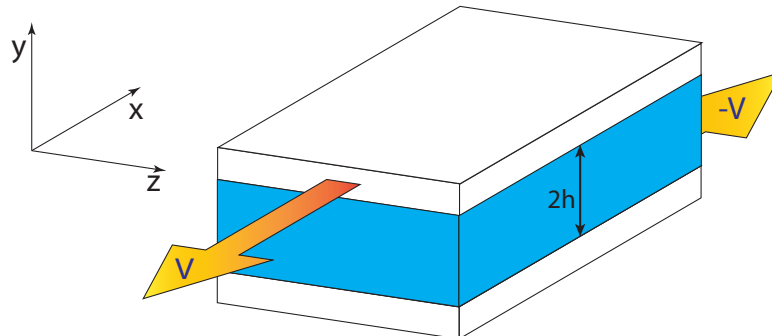


Figure 2: A schematic of the plane Couette geometry. The upper and lower plates (white) extend infinitely in the plane, as does the fluid (blue) filling the gap between them. The upper and lower plates move with some constant velocity, and apply shear stresses to the fluid, resulting in fluid motion. While in general the plates can move in any direction, there is always a reference frame in which the plates move with equal but opposite velocity and it is convenient to work in this reference frame. According to convention, the  $x$  axis is aligned along the plate velocity and is referred to as the **streamwise** direction. The  $y$ -axis is aligned perpendicular to the plates and is referred to as the **wall-normal** direction. The  $z$ -axis is normal to both axes and is referred to as the **spanwise** direction.

velocity of the upper plate. This gives the Reynolds number as

$$Re = \frac{hV}{\nu}, \quad (1)$$

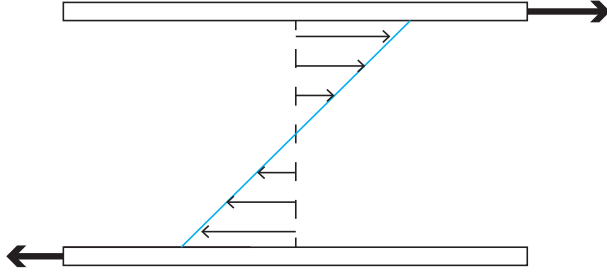


Figure 3: A cross-sectional representation of plane Couette flow, with the linear, laminar velocity profile shown. By symmetry, the laminar profile must be the same everywhere. At the top and bottom, where the fluid meets the walls, no-slip boundary conditions require that the wall-tangent velocity equal the boundary velocity.

where  $\nu$  is the kinematic viscosity of the fluid. When  $Re$  is very small, only the laminar flow state is stable. In the case of plane Couette flow this corresponds to a linear velocity profile, shown in Figure 3. As  $Re$  increases, experiments [6] have demonstrated the existence of long-lived turbulent flows, despite the fact that linear stability analysis predicts that the laminar state should remain stable.

## Tackling Turbulence

The traditional approach for the analysis of turbulent flow is the statistical approach initially developed by Reynolds, Prandtl, von Karman, Kolmogorov and others [7]. At the core of the statistical approach to turbulence is the assumption that turbulent flow states can be expressed as random perturbations around some mean flow. At high  $Re$ , where direct numerical simulation (DNS) of the flow is computationally infeasible,<sup>1</sup> the statistical approach is invaluable. However, at low-to-moderate  $Re$ , these models can become less accurate [7]. Even ignoring the moderate  $Re$  behavior of the statistical models, a fundamental problem with the statistical approach is that it discards much of the dynamical information about turbulence. Some statistical methods like Reynolds Averaged Navier-Stokes choose to time-average the Navier-Stokes equations, while others like Large Eddy Simulations model all small length scale behavior, resolving only large length scales. For this reason, it seems likely that while statistical methods will remain fundamental to applied computational fluid dynamics (CFD), especially in engineering practice, they cannot truly provide an answer to the turbulence problem.

An alternate approach was proposed by Eberhard Hopf in 1948 [8]. Hopf suggested that solutions to the Navier-Stokes equations might be thought of as trajectories in an infinite dimensional state space in which each point corresponded to a possible velocity field. To better understand what this would mean, consider the mean velocity field

---

<sup>1</sup>In essence, this is due to the fact that the minimum computational resolution required for DNS scales as  $Re^{2/25}$  in 3D. As a result, the numerical resolution required to resolve even moderate  $Re$  flows is huge.

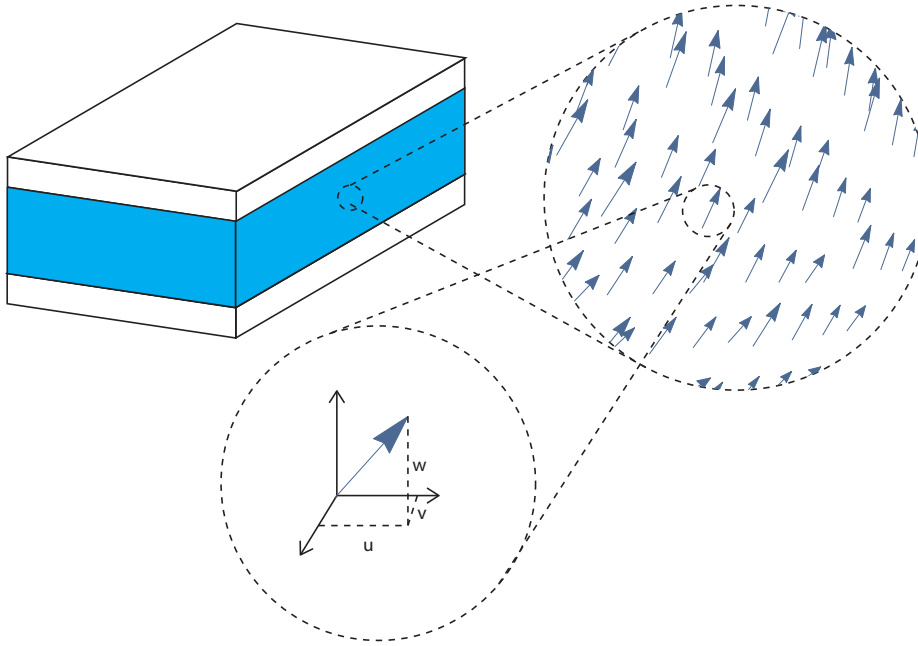


Figure 4: At each point in the fluid volume, the velocity field has a value that is described by three numbers, thus requiring three dimensions to track over time.

of some infinitesimal volume of fluid, pictured in Figure 4. In order to describe the velocity at a point in the fluid, three numbers are required (each of which can take any real value), so this vector lives in a three dimensional vector space. Now any finite fluid volume will have an infinite number of points at which the velocity field has to be specified, so we would need an infinite set of numbers to describe the full velocity field. An object that would keep track of all these numbers would form an infinite dimensional vector  $\mathbf{v} = \{v_{i,1}, v_{i,2}, v_{i,3}\dots\}$ ,  $i \in \mathbb{R}$ , so that any flow state would be represented by a unique vector in this infinite dimensional vector space, which is known as the **state space**.

Luckily, every point in the space does not necessarily correspond to a solution of the Navier-Stokes equation; for a given finite  $Re$ , for instance, the gradient of the velocity field cannot be too large since it would be smoothed out by viscosity. Hopf thus conjectured that physical trajectories corresponding to solutions to the Navier-Stokes equation would lie on some finite-dimensional manifold (known as the **inertial manifold**) embedded within this infinite dimensional space. The restriction of dynamics from the infinite dimensional space to a finite dimensional inertial manifold due to the variation of a control parameter<sup>2</sup> has been rigorously proven under certain conditions [9]. For the Navier-Stokes equation, the inertial manifold's control parameter is  $Re$ , and physical intuition suggests that its structure should also have  $Re$  dependence, since at very low  $Re$ , the only physical solution is the laminar state which corresponds

---

<sup>2</sup>The control parameter of a dynamical system is a number that is time-independent, and typically dictates the behavior of the system in some way. For instance, in the dimensionless simple harmonic oscillator,  $\ddot{x} + 2\zeta\dot{x} + x = 0$ , the control parameter is the dimensionless number  $\zeta$ , whose value determines whether the system is undamped, underdamped, over damped or critically damped.

to a point in the state space. As  $Re$  increases, more complex flows become physically permissible, so the inertial manifold grows from a point of dimension 0 into a more complex, higher dimensional manifold. Hopf proposed that turbulence in this view was simply a trajectory that would travel across wide distances on the inertial manifold.

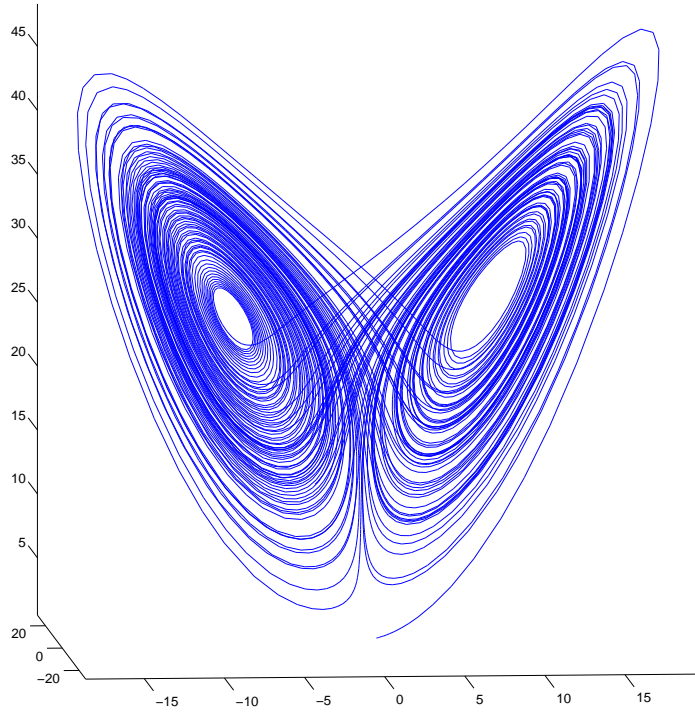


Figure 5: A plot of a trajectory for the Lorenz system. The Lorenz system is an excellent example of a system in which the dynamics collapse onto an inertial manifold - in this case, the dynamics exist on a manifold of fractal dimension 2.06 [2], even though the state space is in three dimensions.

Unfortunately for Hopf, the computer power necessary to pursue this line of work was not available in 1948, leading him to comment in frustration that “the great mathematical difficulties of these important problems are well known and at present the way to a successful attack on them seems hopelessly barred” [8]. It would take until 1963 and the derivation of the Lorenz system (Figure 5) for the first numerical state-space analysis of turbulence [10], albeit for a highly truncated version of

Navier-Stokes, designed to investigate Rayleigh-Bernard convection.<sup>3</sup> There have also been a number of efforts to explore the structure of invariant manifolds in moderate  $Re$  turbulence Navier-Stokes, such as Proper Orthogonal Decomposition [11] and the ‘self-sustaining process theory’ [12], which while fruitful, are nevertheless models of turbulent flow, and not an exact analysis of the Navier-Stokes equations.

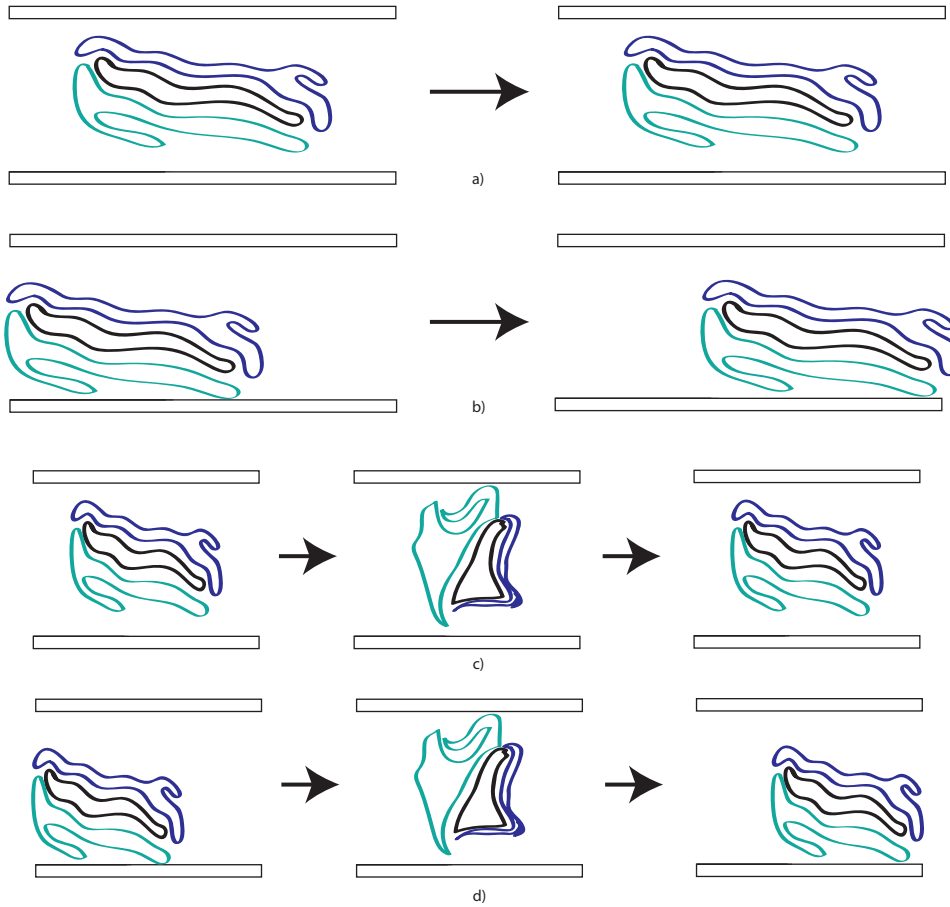


Figure 6: The four main categories of exact coherent structures. In all diagrams, only a particular flow structure is displayed, to demonstrate the various types of exact coherent structures. These could be, for example, isosurfaces of velocity or energy. (a) An equilibrium solution, where the fluid structure does not change over time. (b) A relative equilibrium or traveling wave solution, where the state does not change in its own reference frame, but is translated relative to the observer. (c) A periodic orbit, where the flow state changes over time, but returns to the original state after some period  $T$ . (d) A relative periodic orbit, where the flow state is periodic in its own reference frame, but is translated relative to the observer.

Another avenue of research emerged in 1990, when Nagata computed nontrivial

<sup>3</sup>Interestingly, Lorenz truncated Navier-Stoke via a Galerkin approximation, which is what the simulation library `Channelflow` which features heavily in this thesis also does, though it allows for many more Fourier modes than Lorenz did.

**equilibrium** flow states for plane Couette flow by continuing the wavy vortex solution of Taylor-Couette flow [4]. This class of solutions, which were named **exact coherent structures** by Waleffe [13] are the result of calculating exact, invariant solutions of the fully resolved Navier-Stokes equations. The family of exact coherent structures was expanded with the discovery of **traveling wave equilibria** by Nagata in 1997, the computation of **periodic orbits** by Kawahara and Kida in 2001 [14], and the computation of **relative periodic orbits**<sup>4</sup> by Viswanath in 2007 [15]. Figure 6 summarizes these four categories of exact coherent structures. The ultimate hope of this line of research is that turbulence can be viewed as chaotic trajectories on the inertial manifold that are guided by hyperbolic exact coherent structures<sup>5</sup> (Figure 7).

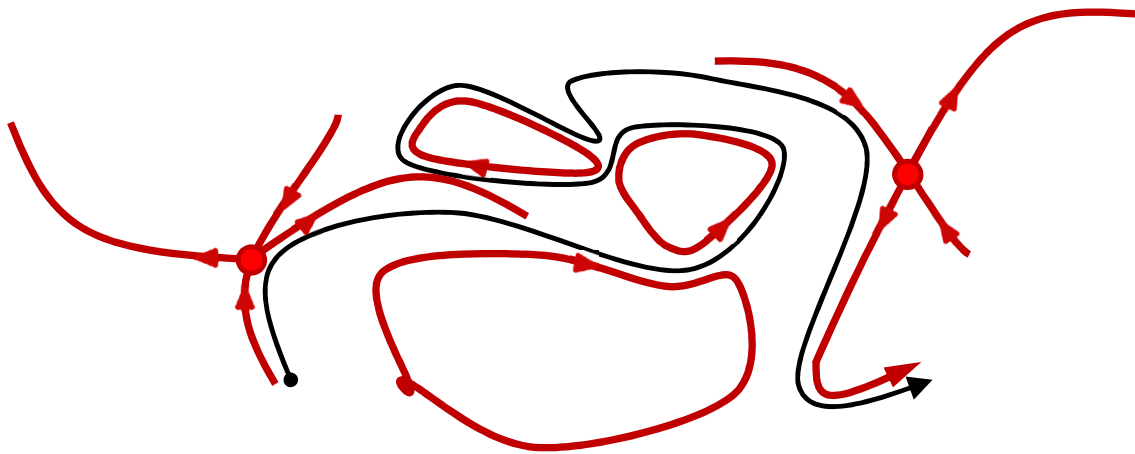


Figure 7: A schematic of a turbulent trajectory in state space and the coherent structures that guide it. (a) A turbulent trajectory in black appears chaotic and unpredictable in isolation. (b) When the underlying coherent structures in red are superimposed, however, the guiding of the dynamics by the exact coherent structures becomes evident. Starting from the left, the trajectory is pulled in towards an equilibrium (filled circle) along its stable manifold (arrow pointing inwards), before being ejected along its unstable manifold (arrow pointing outwards). The trajectory then shadows three periodic orbits, whose stable and unstable manifolds are not trivial to represent visually, but nonetheless exist, before being attracted and ejected by the final equilibrium and continuing on its way. Reproduced from D. Borrero-Echeverry, *Subcritical Transition to Turbulence in Taylor-Couette Flow*, PhD. Dissertation, Dept. of Physics, Georgia Institute of Technology, 2014 [3].

Of the work that has been done in the field, a large proportion of it has been computational, and experiments by Hof et al. and De Lozar et al. [16, 17] provide the only direct experimental verification of the existence of exact coherent structures in

<sup>4</sup>That is, flow states that are periodic after some phase shift

<sup>5</sup>That is to say, the exact coherent structures have many stable directions that are highly attractive and pull trajectories towards them, and a few unstable directions that ultimately eject the trajectory.

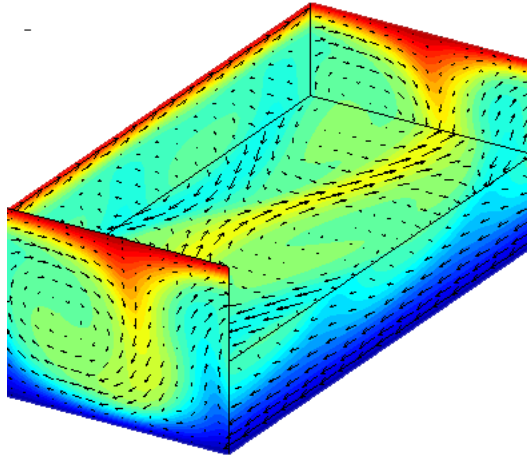


Figure 8: The roll-streak structure of the Nagata upper branch equilibrium [4]. The in-plane velocity vectors in the periodic cell are displayed for the box walls, as well as the mid-plane. The coloration reflects the streamwise velocity, where blue indicates a large streamwise velocity out of the page, and red represents a large streamwise velocity into the page. The vortex that forms the roll is clearly visible on the near box wall, as is the streak running through the midplane of the box. These structural features are often seen in real turbulent flows, and solutions that approach the vicinity of this solution in the state space will take on some of this roll-streak structure.

nature to date. However there have been several indirect results that establish the importance of exact coherent structures in turbulent dynamics. These include the resemblance of Nagata's so-called 'upper branch' equilibrium solution [4] to the roll-streak structure seen in DNS [18] (Figure 8), and the potential role of the stable manifold of its sister lower branch solution in separating the turbulent and laminar basins of attraction [13]. Advances in computing power, along with the development of CFD algorithms, such as `Channelflow` [19], have also made the computation of these structures generally feasible.

In order to compute the first generation of exact coherent structures, researchers placed substantial symmetry constraints on the dynamics. This had the benefit of greatly reducing the computational cost, but has resulted in exact coherent structures that are not necessarily representative of turbulence, since we expect turbulent fields to display little to no symmetry in general. As a result, while the symmetric exact coherent structures appear to inform our understanding of turbulent transitions [5], they do not necessarily inform our understanding of turbulent dynamics. The focus of this thesis has been to find periodic orbits with broken symmetry, and to investigate their properties and how they compare to their unbroken brethren.

In Chapter 1, I will lay out the Navier-Stokes equation and the Couette geometry in further detail. In Chapter 2, I will discuss the symmetries of the Navier-Stokes equations for plane Couette flow and the advantages and disadvantages afforded by

considering symmetric subspaces. Chapter 3 will discuss in detail the spectral methods used to integrate Navier-Stokes forward in time and the Newton-Krylov-hookstep algorithm used to find exact coherent structures in `Channelflow`, along with the workflow used in this thesis. Chapter 4 will present the results of these calculations, which include a new low-period orbit with broken symmetry that exists over a wide range of Reynolds numbers and computational domain sizes. Finally, Chapter 5 will provide a summary of the main ideas and suggests potential topics for future research.



# Chapter 1

## Equations of Flow

Big whorls have little whorls, which  
feed on their velocity, And little  
whorls have lesser whorls, and so on  
to viscosity.

---

Lewis Richardson

### 1.1 Formalisms

If we were to describe the dynamics of a point particle, we would probably begin by writing the total force on the object as a sum of various contributions - thrust, drag, electric, magnetic, gravitational, etc., so that

$$\mathbf{F}_{\text{total}} = \sum_i F_i. \quad (1.1)$$

To relate this back to the **kinematic** variables (position, velocity, etc.), we can then use Newton's Second Law,

$$\frac{d\mathbf{p}}{dt} = \mathbf{F}_{\text{total}}, \quad (1.2)$$

to generate an equation of motion. The trajectory could then be calculated via analytic or numeric integration of (1.2). While in principle we can use this approach to describe the behavior of a large collection of particles making up the fluid, practical considerations prevent us from modeling the behavior of each individual particle, for the following reason – in a milliliter of water, there are approximately  $10^{22}$  water molecules, each with 6 degrees of freedom.<sup>1</sup> Applying (1.2) to all these particles would result in about  $10^{23}$  coupled ordinary differential equations. Such a set of equations would be hard to write down, let alone solve! Clearly, a more intelligent approach is needed. The formalism that I will present here begins by modeling the fluid as a continuum. My derivation is based off that in [20].

---

<sup>1</sup>If we ignore the vibrations of the O-H bonds

### 1.1.1 The Eulerian Formulation

When asked to consider the mechanical evolution of some collection of bodies, two obvious methods would be readily apparent - we could either follow a collection of particles on their way through space and time (the **Lagrangian** formulation), or we could situate ourselves at some point in space and observe the properties of particles that pass through the surrounding region (the **control volume**) over time (the **Eulerian** formulation). The Lagrangian formulation will be familiar to anyone with a basic physics education, since it lends itself readily towards analysis of rigid-body motion. When considering fluids, however, the disadvantages of the Lagrangian formulation (noted above) stand in contrast to the ease of analysis afforded by the Eulerian formulation, which remains as easy (or hard) as it was for rigid body motion.

### 1.1.2 The Fluid Particle

When we use the Eulerian formulation, we cannot know the full timeline of any individual particle over its lifetime – we only know the properties of particles within the control volume. Therefore, the principle quantity in the Eulerian formulation is the velocity field<sup>2</sup>  $\mathbf{v}(\mathbf{x}, t) = v_x(\mathbf{x}, t)\hat{\mathbf{x}} + v_y(\mathbf{x}, t)\hat{\mathbf{y}} + v_z(\mathbf{x}, t)\hat{\mathbf{z}}$ , along with the pressure and density fields, which are the average values of these properties in a control volume surrounding a point.

A subtle issue arises in doing this, however. Since the velocity field is continuous, it has a well-defined value at every point in space, which we would want to be associated with the velocity of a particle at that point in space. However, there are finite number of particles in any collection of fluid with a finite spatial extent. If these particles have some finite volume, then the formulation assigns multiple velocities to a single particle - and if the particles are infinitesimal, then the formulation assigns velocities to empty space! This issue can be resolved by appealing to the continuum hypothesis, which suggests that a control volume (the ‘**fluid parcel**’) can be chosen such that it is large enough to form a meaningful average of the quantities within, but small enough that the properties do not vary significantly over the parcel, and that from a macroscopic perspective, the properties appear continuous.

The reader may ask “Can such a parcel even exist?” As an example, let us consider water, with approximately  $10^{22}$  molecules per cubic centimeter. Imagine our fluid parcels as tiling the volume with cubes with sides of length  $dl$ , giving a total volume of  $dl^3$  per parcel. First, let us make  $dl$  small enough that the macroscopic properties appear continuous - how about one micron? That gives the volume of a fluid particle as one cubic micrometer. For scale, consider that the volume of the human red blood cell ranges from 80-100 cubic micrometers [21] - this seems acceptably small

---

<sup>2</sup>As opposed to particle trajectories  $\mathbf{x}(t)$  in the Lagrangian formulation.

for considering, say, the flow around a ship.<sup>3</sup> The number of water molecules within each fluid parcel is then

$$10^{22}dl^3 = 10^{22} \times 10^{-12} = 10^{10}, \quad (1.3)$$

or about 10 billion water molecules, which is certainly sufficient to achieve a meaningful average. Having defined a fluid parcel in this way allows us to behave as if these macroscopic variables have well-defined values at every point in space, which greatly simplifies the following analysis.

## 1.2 Mass Conservation

While not formally a part of the Navier-Stokes equations (which are a statement about conservation of linear momentum), conservation of mass is nevertheless essential in solving fluid problems, and will serve as a demonstration of the control volume method. Consider a volume  $\Omega$  that is fixed in space and has some mass density  $\rho = \rho(\mathbf{x}, t)$  and a velocity  $\mathbf{v} = \mathbf{v}(\mathbf{x}, t)$  that are generically functions of time and space. This allows us to define the **mass current density**  $\mathbf{m} = \mathbf{v}\rho$ . The mass contained within the volume  $\Omega$  is then given by

$$M = \int_{\Omega} \rho \, dV. \quad (1.4)$$

The flow of mass out of the volume through the surface  $d\Omega$  of  $\Omega$  is given by

$$\mathcal{M}_{flow} = \int_{d\Omega} \mathbf{m} \cdot \mathbf{n} \, dA = \int_{\Omega} \nabla \cdot (\rho \mathbf{v}) \, dV, \quad (1.5)$$

by the divergence theorem. Now in classical physics, mass should not appear or disappear, so the sum of the rate of mass flow into (or out of) the volume and the rate of change of mass inside the volume  $M_{encl}$  must be zero, giving

$$\frac{\partial M_{encl}}{\partial t} + \mathcal{M}_{flow} = 0, \quad (1.6)$$

so that

$$\frac{\partial}{\partial t} \left( \int_{\Omega} \rho \, dV \right) + \int_{\Omega} \nabla \cdot (\rho \mathbf{v}) \, dV = 0. \quad (1.7)$$

Since  $\Omega$  is time-independent, the time derivative commutes with the integral, giving

$$\int_{\Omega} \frac{\partial \rho}{\partial t} + \nabla \cdot (\rho \mathbf{v}) \, dV = 0. \quad (1.8)$$

But  $\Omega$  is arbitrary, so the integrand must be zero everywhere, and mass is conserved if

$$\frac{\partial \rho}{\partial t} + \nabla \cdot (\rho \mathbf{v}) = 0. \quad (1.9)$$

---

<sup>3</sup>The validity of the continuum hypothesis is clearly dependent on the density of the fluid and the length scale of the phenomenon to be modeled, but holds up even for the sparse gas clouds of protoplanetary disks [22] or at the nanoscale [23].

If the flow is (approximately) incompressible, which will be true for small Mach numbers,<sup>4</sup>  $\rho$  must be constant, and (1.9) becomes

$$\nabla \cdot \mathbf{v} = 0. \quad (1.10)$$

## 1.3 Conservation of Linear Momentum

As mentioned earlier, the Navier-Stokes equations are simply a statement of conservation of linear momentum, along with certain assumptions about stress and strain, which are presented below.

### 1.3.1 Stress

Stress is a mathematical entity that contains information about the forces acting on an object. As with force, we define positive stress as stress that acts towards the control volume, and negative if it acts away from it. Unlike force however, stress is not a vector, since it encodes both the force on an object, as well as the plane that force acts in. Since there are three directions and three planes of action, a stress entity generally has nine elements, and can be represented as a **second rank tensor**. For example, the viscous stress tensor  $\mathcal{T}$  is identified by two subscripts, where the first subscript indicates the plane of action, and the second the direction of action. So  $\mathcal{T}_{xy}$  represents the viscous force on the  $(y, z)$  plane acting in the  $y$  direction.

### 1.3.2 Strain

Now that we can consider the forces on a fluid particle, we need to link these forces back to the observable quantities in the form of strain, a second rank tensor which encodes information about how the fluid packet deforms under stress. In solids, this is easy - Hooke's Law for elastic substances, for instance, sets the strain proportional to the stress:

$$\sigma = \mathcal{C}\epsilon, \quad (1.11)$$

where  $\sigma$  is the Cauchy stress tensor,  $\mathcal{C}$  is the (fourth rank) stiffness tensor and  $\epsilon$  is the infinitesimal strain tensor. However, for fluids, this is not the case - you can imagine that if you applied a constant force to a cube of water, it would deform continuously, without offering any resistance. Newton theorized that for continuously deformable fluids, the 1-D relationship between stress  $\mathcal{T}$  and strain  $\mathcal{S}$  should have the following form:

$$\mu \frac{d\mathcal{S}}{dt} = \mu \frac{du}{dx} = \mathcal{T}, \quad (1.12)$$

where  $\mu$  is the fluid viscosity and  $u$  is the velocity. Stokes extended this to three dimensions, giving the Newtonian constitutive relationship between stress and strain

---

<sup>4</sup>The Mach number is the ratio of the fluid velocity to the speed of sound in the fluid. For reference, the speed of sound in water is  $1497 \text{ ms}^{-1}$  at room temperature and pressure, so for many practical purposes, water can be considered incompressible.

(for an incompressible fluid):

$$\mathcal{T}_{ij} = -P\delta_{ij} + \mu \left( \frac{\partial u_i}{\partial x_j} + \frac{\partial u_j}{\partial x_i} \right), \quad (1.13)$$

where  $\delta_{ij}$  is the Kronecker delta function<sup>5</sup> and  $P$  is the pressure. A fluid obeying Newton's constitutive relation is called a Newtonian fluid. Water, and most gases under normal conditions are Newtonian, but fluids like blood, quicksand and corn starch (to name a few) are not. In this thesis, we will restrict ourselves to Newtonian fluids.

### 1.3.3 Surface Forces

Having written down the stress tensor  $\mathcal{T}$  as a function of the velocity field, we can now link it to the surface forces on a fluid particle. Recalling that stresses act over  $d\Omega$  of the fluid particle, the total surface force from stress is then simply

$$\mathbf{F}_s = \int_{d\Omega} \mathcal{T} \cdot \mathbf{n} \ dA, \quad (1.14)$$

where  $\mathbf{n}$  is the surface normal.

### 1.3.4 Newton's Second Law

For a fluid parcel  $\Omega$ , Newton's Second Law can be rewritten as

$$\sum \mathbf{F}_{\text{total}} = \int_{\Omega} \frac{\partial \rho \mathbf{u}}{\partial t} \ dV \quad (1.15)$$

where the sum is over all possible external forces. We can further split  $\mathbf{F}$  into two kinds of forces - body forces, like gravity or electromagnetism, and surface forces from stresses. We group the body forces  $\mathbf{F}_b$  as

$$\mathbf{F}_b = \int_{\Omega} \rho \mathbf{f} \ dV, \quad (1.16)$$

where  $\mathbf{f}$  is the **body force density**. Using (1.14) to express the surface forces, (1.15) becomes

$$\int_{\Omega} \rho \mathbf{f} - \frac{\partial \rho \mathbf{u}}{\partial t} \ dV + \int_{d\Omega} \mathcal{T} \cdot \mathbf{n} \ dA = 0. \quad (1.17)$$

This can be written in differential form using the same trick used to generate (1.9), giving Cauchy's Equation of Motion

$$\rho \mathbf{f} - \frac{\partial \rho \mathbf{u}}{\partial t} + \nabla \cdot \mathcal{T} = 0. \quad (1.18)$$

---

<sup>5</sup> $\delta_{ij} = 1$  if  $i = j$  and 0 otherwise

From this, the incompressible Navier-Stokes equation arise by a substitution of (1.13) into (1.18), giving (after tedious rearrangement by components),

$$\frac{\partial \mathbf{u}}{\partial t} + (\mathbf{u} \cdot \nabla) \mathbf{u} = \mathbf{f} - \frac{1}{\rho} \nabla P + \frac{\mu}{\rho} \nabla^2 \mathbf{u}. \quad (1.19)$$

By using the substitutions

$$\mathbf{x} \Rightarrow L\mathbf{x} \quad (1.20)$$

$$\mathbf{u} \Rightarrow U\mathbf{u} \quad (1.21)$$

$$t \Rightarrow \frac{L}{U} t \quad (1.22)$$

$$P \Rightarrow \rho U^2 P, \quad (1.23)$$

and neglecting body forces, we obtain the nondimensional version of (1.19) –

$$\frac{\partial \mathbf{u}}{\partial t} + (\mathbf{u} \cdot \nabla) \mathbf{u} = -\nabla P + \frac{1}{Re} \nabla^2 \mathbf{u}, \quad (1.24)$$

$$\nabla \cdot \mathbf{u} = 0, \quad (1.25)$$

where

$$Re = \frac{UL\rho}{\mu}. \quad (1.26)$$

In practice, the values of  $L$  and  $U$  are chosen by convention to reflect the natural length and velocity scales of the problem at hand.

## 1.4 Plane Couette Flow

Since plane Couette flow is a shear driven flow, we set the pressure gradient to zero and use no-slip boundary conditions at the walls, which sets the surface tangential velocity equal to the surface velocity. The Navier-Stokes equation for plane Couette flow is then given by

$$\frac{\partial \mathbf{u}}{\partial t} + (\mathbf{u} \cdot \nabla) \mathbf{u} = \frac{1}{Re} \nabla^2 \mathbf{u}, \quad (1.27)$$

with boundary conditions

$$\mathbf{u}(x, \pm 1, z, t) = (\pm 1, 0, 0), \quad (1.28)$$

and

$$\frac{\partial}{\partial y} \mathbf{u}(x, \pm 1, z, t) = (a, 0, b), \quad (1.29)$$

for some constant  $a$  and  $b$  and geometry as pictured in Figure 2. We nondimensionalize by the velocity  $V$  of either plate and the half-plate distance  $h$ , so that the Reynolds number is given by

$$Re = \frac{hV\rho}{\mu}. \quad (1.30)$$

In order to derive the laminar velocity profile shown in Figure 3, note that at very low  $Re$ , the right hand side of (1.27) dominates. If we assume that the flow is unidirectional and steady, so that  $\mathbf{u} = u_x \hat{\mathbf{x}}$ , symmetry considerations tell us that the velocity field can only be a function of height, so that the Navier-Stokes equation reduces to

$$\frac{\partial^2 u_x}{\partial y^2} = 0. \quad (1.31)$$

This has a solution of the form

$$\mathbf{u}(y) = y \hat{\mathbf{x}}, \quad (1.32)$$

which corresponds to the laminar flow profile shown in Figure 3. Consider then a perturbation  $\mathbf{v}(x, y, z, t)$  away from the laminar state, so that the initial field is  $\mathbf{u}(x, y, z, t) = \mathbf{v}(x, y, z, t) + y \hat{\mathbf{x}}$ . Substituting this into (1.24), we get

$$\frac{\partial \mathbf{v}}{\partial \tau} + y \frac{\partial \mathbf{v}}{\partial x} + v \hat{\mathbf{x}} + (\mathbf{v} \cdot \nabla) \mathbf{v} = \frac{1}{Re} \nabla^2 \mathbf{v}, \quad (1.33)$$

$$\nabla \cdot \mathbf{v} = 0. \quad (1.34)$$

Adapting the no-slip boundary conditions from (1.28) and no-penetration boundary from (1.29), we get

$$\mathbf{v}(x, \pm 1, z, t) = 0, \quad (1.35)$$

$$\frac{\partial}{\partial y} \mathbf{v}(x, \pm 1, z, t) = (a, 0, b). \quad (1.36)$$

At this point we need to introduce artificial boundary conditions to render the infinite planar domain computationally tractable. We enforce the periodic boundary conditions

$$\mathbf{v}(x, y, z, t) = \mathbf{v}(x + L_x, y, z, t), \quad (1.37)$$

$$\mathbf{v}(x, y, z, t) = \mathbf{v}(x, y, z + L_z, t), \quad (1.38)$$

where  $L_x$  and  $L_z$  are the lengths of the periodic cell. This gives the complete equation of motion for the perturbing velocity field. Since the laminar profile is steady, understanding the turbulent field's trajectory in state space now reduces to understanding the behavior of the turbulent perturbation, and the structure of its inertial manifold. (1.33) is not generally analytically integrable, so we must tackle it numerically. Before presenting the numerical methods and workflow, however, I will take a slight detour to discuss in detail the symmetries of the plane Couette flow problem, as they are a central part of the work to follow.



# Chapter 2

## Symmetry in plane Couette flow

Tyger! Tyger! Burning bright,  
In the forests of the night.  
What immortal hand or eye,  
Could frame thy fearful symmetry?

---

William Blake, *The Tyger*

The dynamical behavior of a physical system often displays symmetry. The electron wavefunction in the ground state of hydrogen, or the gravitational motion of a planet around a star, for instance, display very high degrees of spatial symmetry. Understanding the symmetries of a system can be incredibly useful to an investigator, since they hint at conserved physical quantities (through Noether's Theorem), and can greatly reduce the complexity of the system in various ways. In order to further discuss symmetry, it will be useful to introduce some terminology, following the conventions in [24].

**Definition 1.** A **group**  $(G, *)$  is an object that contains a set  $G$  and a binary operator known as the **group law**  $* : G \times G \rightarrow G$  that has the following properties

1. **Closure:** For every  $a, b \in G$ ,  $a * b \in G$ ,
2. **Associativity:** For every  $a, b, c \in G$ ,  $a * (b * c) = (a * b) * c$ ,
3. **Identity:** There exists a so-called identity  $e \in G$  such that for any  $a \in G$ ,  
$$e * a = a,$$
4. **Inverse:** For all  $a \in G$ , there exists an inverse  $a^{-1} \in G$  such that  $a * a^{-1} = a^{-1} * a = e$ .

and has a group action  $\star : G \times A \rightarrow A$  on a set  $A$  such that

1. **Associativity** For all  $a, b \in G$  and  $\alpha \in A$ ,  $a \star (b \star \alpha) = (a \star b) \star \alpha$ ,
2. **Identity** For all  $\alpha \in A$ ,  $e \star \alpha = \alpha$ .

**Definition 2.** The **order** of a group  $(G, *)$  is the number of elements in  $G$ .

**Definition 3.** A **subgroup**  $(H, *)$  of  $(G, *)$  is a group such that  $H \subseteq G$ .

**Definition 4.** A **dynamical system** is an object  $(R, X, T)$ , where  $X$  is the state space,  $T$  is a set of times, and  $R : X \times T \rightarrow X$  is a function that describes how a state evolves in time. That is,  $x' = R_t(x) \in X$  describes the state that the initial condition  $x \in X$  evolves to after a time  $t \in T$ . If  $X$  and  $f$  are continuously differentiable with time, then

$$\frac{\partial}{\partial t} R_t(x)|_{t=0} = f(x), \quad (2.1)$$

so that the set of points an initial condition evolves through (known as the **trajectory**) is described by the ordinary differential equation (ODE)

$$\frac{dx}{dt} = f(x). \quad (2.2)$$

I will refer to a dynamical system by its ODE, with the understanding that it applies to all  $x \in X$ .

**Definition 5.** A **symmetry group** for a dynamical system  $\dot{x} = f(x)$  is the group  $(\Sigma, *)$  such that for any linear transformation  $\sigma \in \Sigma$ ,

$$\sigma \star \dot{x} = \sigma \star f(x) = f(\sigma \star x). \quad (2.3)$$

Such a linear transformation is said to be a symmetry transformation, and the dynamical system that satisfies (2.3) is said to be  **$\Sigma$ -equivariant**.

**Definition 6.** For a particular state  $\mathbf{u}$  in the state space of  $\dot{x} = f(x)$ , a symmetry group  $(\Sigma, *)$  such that for all  $\sigma \in \Sigma$ ,

$$\sigma \mathbf{u} = \mathbf{u} \quad (2.4)$$

is known as the **isotropy subgroup** of  $\mathbf{u}$ , and  $\mathbf{u}$  is said to **satisfy** or be **fixed** by  $\Sigma$ .

**Definition 7.** If a group  $(G, *)$  has the further property that for all  $a, b \in G$ ,  $a * b = b * a$ , then the group is **abelian**

**Definition 8.** Two subgroups  $(J, *)$  and  $(H, *)$  of  $(G, *)$  are considered **conjugate** if for some  $a \in G$ ,

$$a * J * a^{-1} = H. \quad (2.5)$$

A set of mutually conjugate groups makes up a **conjugacy class**, and since the action of members of a conjugacy class on a particular state  $\mathbf{u}$  can be considered equivalent,<sup>1</sup> only one representative member of a conjugacy class needs to be considered.

**Definition 9.** A set  $\mathcal{G}$  is said to **generate** a group  $(G, *)$  if repeated applications of the group law between elements of  $\mathcal{G}$  produces all the elements of  $G$ .

The symmetry relations of plane Couette flow are discussed extensively in [25, 5], but I will present them here for the sake of flow.<sup>2</sup> To keep notation compact, the group action and group law operator will be omitted and can be inferred from context, and a group  $(G, *)$  will be referred to by the set  $G$ .

---

<sup>1</sup>Since conjugate groups are essentially related by a coordinate transformation [25]

<sup>2</sup>haha

## 2.1 Unbounded Navier-Stokes

If we do not impose boundary conditions on the 3D Navier-Stokes equations on an infinite domain, the system will be equivariant under the group of continuous rotational and translational symmetry transformations, as well as the discrete **pointwise inversion** symmetry transformation  $\sigma_{xz}$  [26], which has the following action on the system:

$$\sigma_{xz}\mathbf{u}(\mathbf{x}) = -\mathbf{u}(-\mathbf{x}) \quad (2.6)$$

While the rotation or translation transformation can be easily conceptualized, the pointwise inversion transformation can provide some difficulty. The easiest way of visualizing the transformation is to view it in a 2D domain instead of in the full 3D, as shown in Figure 2.1.

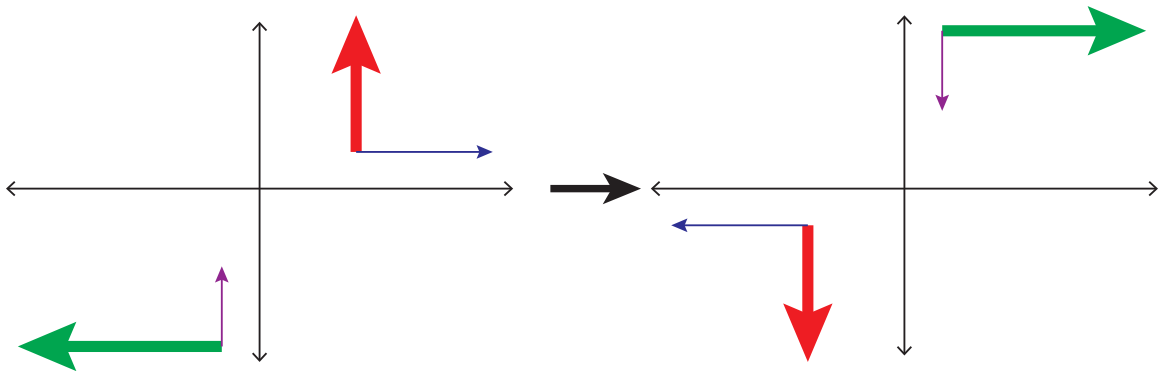


Figure 2.1: A 2D pointwise inversion operation on two sets of vectors according to (2.6).

## 2.2 Plane Couette Flow

If the domain is limited to  $\mathbb{R}^2 \times [-1, 1]$  with the boundary conditions of plane Couette flow, we lose some of the symmetry transformations of the full, unrestricted problem, leaving us with two basic discrete symmetries: a rotation by  $\pi$  about the  $z$  axis (denoted  $\sigma_x$ ) and a reflection about the  $z$  axis (denoted  $\sigma_z$ )<sup>3</sup>, together form a discrete symmetry group  $D = D_{1,x} \times D_{1,z} = \{e, \sigma_x\} \times \{e, \sigma_z\} = \{e, \sigma_x, \sigma_z, \sigma_{xz}\}$  of order 4, where

$$\sigma_x[u, v, w](x, y, z) = [-u, -v, w](-x, -y, z) \quad (2.7)$$

$$\sigma_z[u, v, w](x, y, z) = [u, v, -w](x, y, -z) \quad (2.8)$$

$$\sigma_{xz}[u, v, w](x, y, z) = [-u, -v, -w](-x, -y, -z) \quad (2.9)$$

---

<sup>3</sup>The motivation for these subscripts will become apparent shortly.

We also lose the general rotation and translational symmetries, keeping only the two parameter streamwise-spanwise translations. If we then enforce periodic boundary conditions, these take the form of a continuous  $SO(2) \times SO(2)$  symmetry group

$$\tau_x(l_x)[u, v, w](x, y, z) = [u, v, w](x + l_x, y, z), \quad (2.10)$$

$$\tau_z(l_z)[u, v, w](x, y, z) = [u, v, w](x, y, z + l_z), \quad (2.11)$$

$$\tau_x z[u, v, w](x, y, z) = \tau_x \tau_z[u, v, w](x, y, z). \quad (2.12)$$

The complete symmetry group is then any combination of these symmetry operations, given by  $\Sigma = SO(2)_x \ltimes D_{1,x} \times SO(2)_z \ltimes D_{1,z}$ .<sup>4</sup>

## 2.3 Properties and Isotropy Subgroups of $\Sigma$

It should be evident that since plane Couette flow is equivariant under the continuous translations given in (2.10), solutions can take the form of traveling waves or relative periodic orbits: that is, there exists a different reference frame in which such trajectories are regular equilibria or periodic orbits. However, an initial condition that is fixed by  $\sigma_z$  cannot be translated in the spanwise direction without losing  $\sigma_z$  symmetry (except for the trivial case where  $\frac{\partial \mathbf{u}_z}{\partial z} = 0$ ). Similarly, an initial condition that is fixed by  $\sigma_x$  cannot be translated in the streamwise direction without losing  $\sigma_x$  symmetry (and an initial condition that is fixed by  $\sigma_{xz}$  symmetry cannot be translated at all without losing  $\sigma_{xz}$  symmetry). Since these symmetries are also invariant,<sup>5</sup> a trajectory with one of the discrete symmetries cannot be a traveling wave in the direction corresponding to its subscript.

The presence of the periodic boundary conditions also implies that all solutions are fixed by a translation  $\tau(L_x, 0)$  and  $\tau(0, L_z)$  that corresponds to shifting by a whole box length. However, solutions can also be fixed by any rational translation of the form  $\tau(\alpha L_x, \beta L_z)$ , where  $\alpha, \beta \in \mathbb{Q}$ , or by continuous translations. If we fix  $\mathbf{u}$  by a continuous translation, we force it to have a zero derivative along that axis,<sup>6</sup> and such solutions tend to be uninteresting as they are equivalent to lower-dimensional problems. If  $\mathbf{u}$  is fixed instead by rational translations, the periodic cell is tiled with repeating subcells, as in Figure 2.2. This implies that we can restrict ourselves to isotropy subgroups that are not generated by pure translations.

There is one further reason to restrict the translation symmetry - the unrestricted  $\Sigma$  is not an abelian group, as demonstrated in Figure 2.3, so the order in which symmetry transformations are applied matters. This is undesirable, since it makes the classification of groups slightly more complex, especially when trying to sort groups into their conjugacy classes. From (2.7–2.10) however, it is evident that the

<sup>4</sup>Here,  $\ltimes$  is the semidirect product.

<sup>5</sup>That is, if the symmetry is satisfied at time  $t = t_0$ , it must be satisfied for all times. This is trivially true from Definition 5.

<sup>6</sup>That is, if we fix  $\mathbf{u}$  by  $\tau(l_x, 0)$  for any real  $l_x$ , then  $\frac{\partial \mathbf{u}}{\partial x} = 0$ , and similarly for  $z$ .

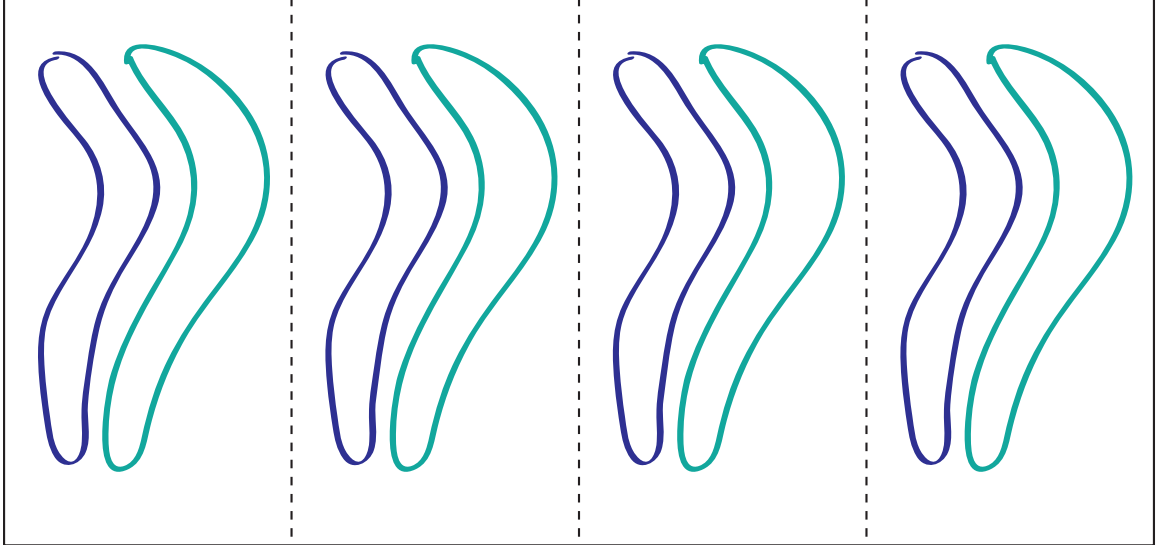


Figure 2.2: If the flow state is fixed by  $\tau(\frac{1}{4}L_x, 0)$ , then the solution will have four repeating streamwise subcells, and it becomes more efficient to solely consider the subcell.

following relation between the  $\sigma$  and  $\tau$  holds:

$$\sigma_i \tau_i = \tau_i^{-1} \sigma_i, \quad (2.13)$$

where  $i$  can index the  $x, z$  or  $xz$  symmetries. Right-multiplication by  $\tau_i$  yields

$$\sigma_i \tau_i^2 = \tau_i^{-1} \sigma_i \tau_i. \quad (2.14)$$

If  $\tau_i$  is restricted to *half*-box shifts, then (2.14) becomes

$$\sigma_i \tau_{i,2}^2 = \sigma_i \tau_{i,1} = \sigma_i = \tau_{i,2}^{-1} \sigma_i \tau_{i,2}, \quad (2.15)$$

where  $\tau_{i,n} = \tau_i(L_i/n)$  represents the spatial periodicity imposed by  $\tau$ . Right multiplication by  $\tau_{i,2}$  yields

$$\tau_{i,2} \sigma_i = \sigma_i \tau_{i,2}. \quad (2.16)$$

So if  $\tau$  is restricted to half-integer box shifts,  $\Sigma$  becomes  $\Sigma_2$ , which is an abelian group, as demonstrated in Figure 2.4.<sup>7</sup> The subgroups of  $\Sigma_2$ , which form the isotropy subgroups we consider for plane Couette flow, are of order  $\{1, 2, 4, 8, 16\}$ . There is only one order 1 subgroup:  $\{e\}$ , which is the typical isotropy group for turbulent flows.<sup>8</sup> There are 15 subgroups of order 2, 35 subgroups of order 4, 15 subgroups of order 8, and one subgroup of order 16, giving 67 subgroups. Luckily, consideration of conjugacy classes greatly lowers the number of subgroups we need to consider. As an example, consider the subgroups  $\{e, \sigma_x\}$  and  $\{e, \sigma_x \tau_{x,2}\}$ .

<sup>7</sup>Note that this also implies that  $\tau_{i,2}$  is its own inverse.

<sup>8</sup>Since they lack any symmetry.

**Theorem 1.** The subgroups  $\{e, \sigma_x\}$  and  $\{e, \sigma_x \tau_{x,2}\} \subset \Sigma_2$  belong to the same conjugacy class.

*Proof.* Following Definition 8, choose  $a = \tau_{x,4} \in \Sigma$ . Then

$$\tau_{x,4}^{-1} \{e, \sigma_x\} \tau_{x,4} = \{\tau_{x,4}^{-1} \tau_{x,4}, \tau_{x,4}^{-1} \sigma_x \tau_{x,4}\} = \{e, \tau_{x,4}^{-1} \sigma_x \tau_{x,4}\}. \quad (2.17)$$

But by (2.14),

$$\tau_{x,4}^{-1} \sigma_x \tau_{x,4} = \sigma_x \tau_{x,2}. \quad (2.18)$$

So  $\{e, \sigma_x\}$  and  $\{e, \sigma_x \tau_{x,2}\}$  belong to the same conjugacy class.  $\square$

So there are only eight conjugacy classes of order 2, with representatives generated by  $\tau_x, \tau_z, \tau_{xz}, \sigma_x, \sigma_z, \sigma_{xz}, \sigma_x \tau_z, \sigma_z \tau_x$ . The conjugacy classes of pure translations can be disregarded, since they are equivalent to considering smaller cells, so we are left with five order 2 conjugacy classes. Of these, the two generated by  $\sigma_x$  and  $\sigma_x \tau_z$  do not permit streamwise traveling waves, the two generated by  $\sigma_z$  and  $\sigma_z \tau_x$  do not permit spanwise traveling waves, and one generated by  $\sigma_{xz}$  permits no traveling waves at all. Furthermore, groups of higher order do not have any conjugacy classes that permit symmetry breaking, so we will, where possible, ignore those groups entirely, since our goal is to find exact coherent structures that have broken symmetry. It is nevertheless important to introduce the order 4 group,  $S = \{e, \sigma_z \tau_x, \sigma_x \tau_{xz}, \sigma_{xz} \tau_z\}$ , as it has been the isotropy subgroup considered by many previous investigators [25], and is used as a starting point for some of the results in this thesis. The important exact coherent structures reported in this thesis have isotropy subgroups  $S_x = \{e, \sigma_x\} \times \{e, \tau_{xz}\}$  and  $S_z = \{e, \sigma_z \tau_{xz}\}$ . Having laid out the theoretical framework for plane Couette flow and exact coherent structures, I will now discuss the numerical method by which the Navier-Stokes equations are integrated, and exact coherent structures are found.

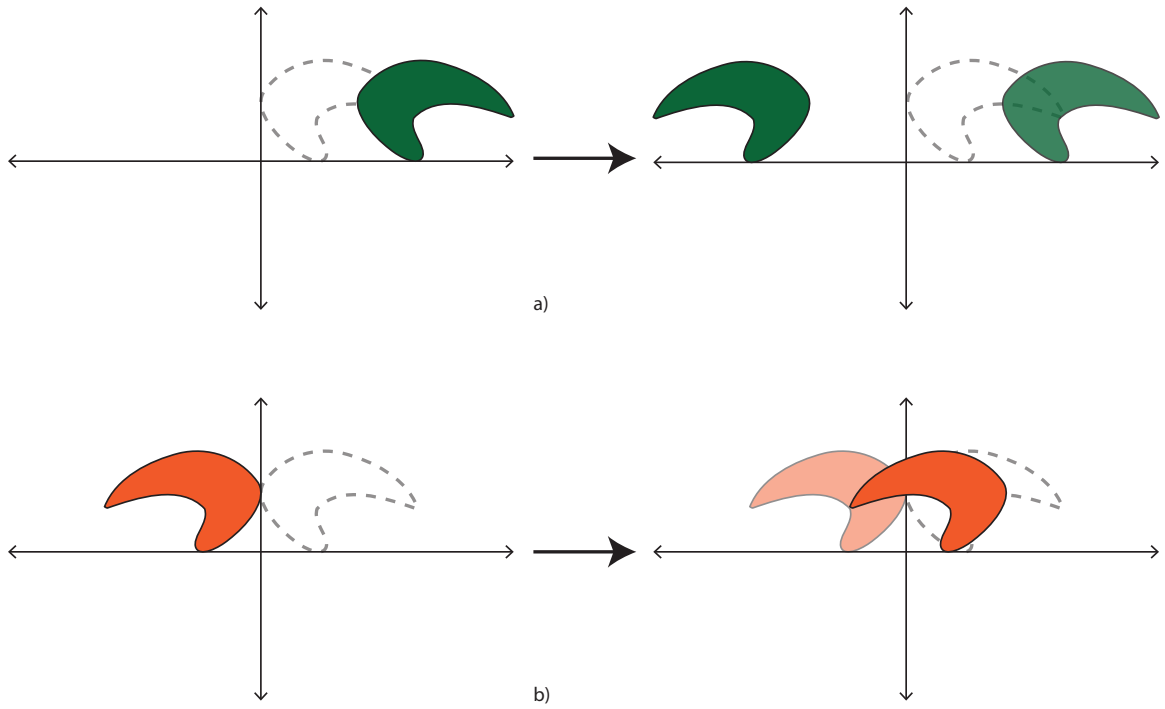


Figure 2.3: A simple demonstration that shifts and reflections do not commute in general. a) An object with a dashed outline is translated to the right, and then reflected across the vertical. b) The same object is reflected before it is translated to the right. Notice that the final positions of the object are not the same.

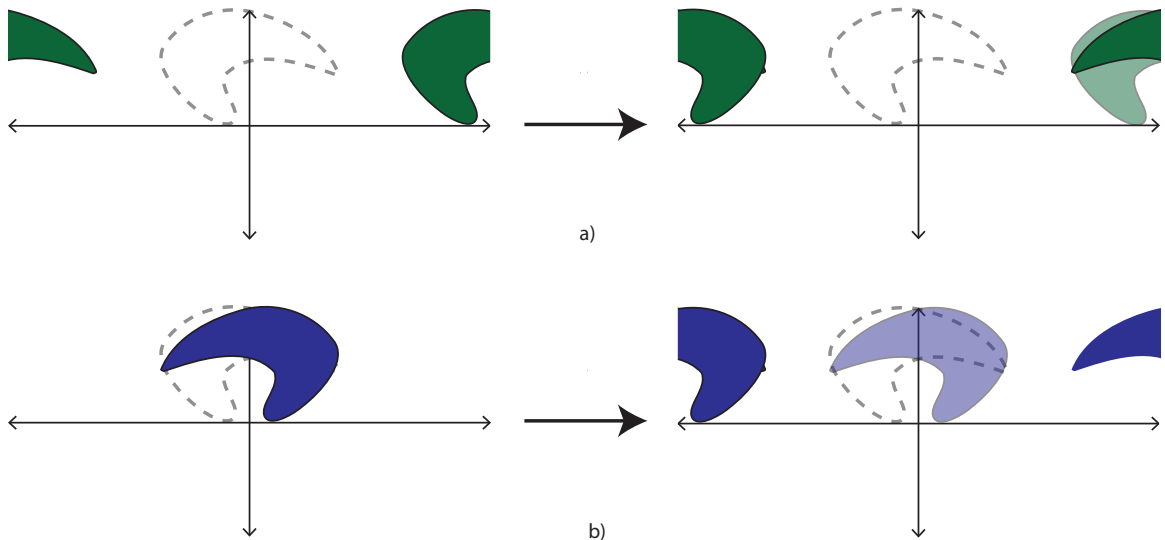


Figure 2.4: When periodic boundary conditions are imposed and translations are restricted to half-period lengths, shifts and reflects commute. a) An object is shifted and then reflected across the vertical. b) The same object is reflected across the vertical and then shifted. The final positions are the same, even if the intermediaries are not.



# Chapter 3

## Numerics and Workflow

On two occasions I have been asked, “Pray, Mr. Babbage, if you put into the machine wrong figures, will the right answers come out?” ... I am not able rightly to apprehend the kind of confusion of ideas that could provoke such a question.

---

Charles Babbage, Passages from the Life of a Philosopher

Computational studies of the Navier-Stokes equations, especially as a dynamical system, are difficult for many reasons, but most important among them is the high degree of complexity inherent in the numerical tools required to maintain efficiency. As mentioned earlier, the two major approaches towards simulating Navier-Stokes are modeling, where some assumptions are made to reduce the complexity of the simulation, and direct numerical simulation (DNS), where no assumptions beyond those used to derive the Navier-Stokes equations and those used to set up the boundary conditions are made. DNS is naturally more accurate (since the physicality of some modeling assumptions can be suspect), but in order to fully resolve the Navier-Stokes equations, it is significantly more computationally expensive than modeling. For this reason, I use the open source library `Channelflow` [19], which has been essential in making any headway in this thesis. `Channelflow` is a spectral DNS library, with additional utilities to find, parametrically continue, and analyze exact coherent structures, which I will lay out in some detail below.

### 3.1 The Spectral Method

#### 3.1.1 The Residual

Spectral methods are part of a larger class of numerical methods known as **weighted residual methods**. In this class of methods, functions are approximated by a truncated series expansion, with the restriction that a quantity related to the residual be

zero (instead of the residual itself). The quantity used in spectral methods is the scalar product

$$\langle u, v \rangle_w = \int_a^b uvw \ dx, \quad (3.1)$$

where  $u(x), v(x)$  are some functions on the interval  $[a, b]$ , and  $w(x)$  is a weighting function.<sup>1</sup> If we then imagine some platonic function (the function that is to be approximated)  $u(x)$  that we attempt to approximate via a finite series expansion, so that

$$u_K(x) = \sum_{k=0}^K \hat{u}_k \psi_k(x), \quad (3.2)$$

for some set of orthonormal basis functions  $\psi_k(x)$ , the residual is then given by

$$R_K = u(x) - u_K(x). \quad (3.3)$$

For a differential equation

$$Du = f, \quad (3.4)$$

where  $D$  is some arbitrary differential operator and  $f(x)$  is some arbitrary source function, the residual is defined

$$R_K = Du_K - f. \quad (3.5)$$

While it may seem logical to require  $R_K = 0$ , this is not possible in general for finite  $K$ , so we instead require that for a set of test functions  $\phi_i(x)$  and weighting function  $w^*$ , the residual satisfies

$$\langle R_K, \phi_i(x) \rangle_{w^*} = 0, \quad (3.6)$$

for some set of  $x_i$ . If  $\phi_i(x) = \delta(x - x_i)$  and  $w^* = 1$ , where

$$\delta(x - x') = \begin{cases} 0 & \text{if } x \neq x' \\ \infty & \text{if } x = x', \end{cases} \quad (3.7)$$

and

$$\int_{-\infty}^{\infty} \delta(x - x') = 1 \ dx, \quad (3.8)$$

then we have the **collocation method**, which forces the approximation to match the platonic function at a set of points. If  $\phi_i(x) = \psi_i(x)$  and  $w^* = w$ , then we have the **Galerkin method**, which forces the mean residual to be zero.

---

<sup>1</sup> $w(x)$  is usually chosen on a case-by-case basis for a particular basis function, and is used to ensure orthonormality.

### 3.1.2 Basis Functions

In the spectral method, trigonometric functions are chosen as the basis. The advantage of trigonometric functions over polynomials is the rapid convergence of the series coefficients – the Fourier coefficients converge exponentially fast, so we can achieve extremely high accuracy with a lower number of modes [27]. However, spectral methods are inappropriate when the boundary geometry is highly complex, as is the case in the majority of industrial applications, where more general weighted residual methods are used. Since the plane Couette geometry is relatively simple, **Channelflow** can make good use of the superior convergence rate of the spectral decomposition. **Channelflow** uses Fourier series in the streamwise-spanwise directions, where the basis functions, weighting functions and spectral projection are given by

$$F_k(x) = e^{ikx}, \quad (3.9)$$

$$w(x) = 1, \quad (3.10)$$

$$u_K(x) = \sum_{k=-K}^K \hat{u}_k e^{ikx}, \quad (3.11)$$

for both  $x$  and  $z$ . Chebyshev polynomials of the first kind are in the wall-normal direction, where the basis functions, weighting functions and spectral projection are given by

$$T_k(x) = \cos(k \cos^{-1}(x)), \quad (3.12)$$

$$w(x) = \frac{1}{\sqrt{1-x^2}}, \quad (3.13)$$

$$u_N(x) = \sum_{k=0}^{(2k-1)/2} \hat{u}_k T_k(x). \quad (3.14)$$

The Fourier series expansion is particularly nice since the derivative  $\partial_x F_k(x) = ikF_k(x)$  is especially easy to calculate, as are the Fourier coefficients by virtue of the Fast Fourier Transform, which is implemented in the Fastest Fourier Transform in the West (FFTW) library [28].

For Chebyshev polynomials, the derivative is slightly more complicated, since

$$\partial_x T_k(x) = 2k \sum_{n=0}^{(2k-1)/2} \frac{1}{c_{k-1-2n}} T_{k-1-2n}(x), \quad (3.15)$$

where  $c_k = 1$  if  $k = 1$  and  $2$  if  $k > 1$ . Since the derivative of a single Chebyshev term becomes a sum of Chebyshev terms, the derivative of the Chebyshev representation

of a function

$$\partial_x \sum_{k=0}^K \hat{u}_k T_k(x) = \sum_{k=0}^K \hat{u}_k^{(1)} T_k(x), \quad (3.16)$$

$$\hat{u}_k^{(1)} = \frac{2}{c_k} \sum_{\substack{p=k+1 \\ (p+k) \text{ odd}}}^K p \hat{u}_p, \quad k \neq K, \quad (3.17)$$

$$\hat{u}_K^{(1)} = 0. \quad (3.18)$$

As with the Fourier decomposition, however, Chebyshev coefficients can be calculated by a discrete cosine transform [5], which is a special case of the discrete Fourier transform, and is thus also computed efficiently by the FFTW.

While Fourier expansions are the easiest to deal with, they are best used on periodic boundaries, since the imposition of aperiodic boundary conditions on a Fourier series expansion can lead to Gibbs oscillations that can make the simulation unphysical [27]. For this reason, the velocity field is expanded as a Fourier series in the plane, and as a Chebyshev polynomial in the wall-normal direction. Chebyshev polynomials can also easily satisfy the no-slip and no-penetration conditions (1.28–1.29), and through the selection of the Gauss-Lobatto grid

$$x_k = \cos\left(\frac{k\pi}{K}\right), \quad k = 0, 1, \dots, K, \quad (3.19)$$

naturally resolve the Navier-Stokes equations more accurately near the boundaries, where the increased accuracy is desirable. The velocity field is then represented as

$$\mathbf{u}_{KJL}(x, y, z) = \sum_{k=-K}^K \hat{u}_k(x) e^{ikx} \sum_{j=-J}^J \hat{u}_j(z) e^{ijz} \sum_{l=0}^L \hat{u}_l(y) T_l(y). \quad (3.20)$$

### 3.1.3 Spatio-Temporal Discretization

Under the (Galerkin) spectral approximation

$$\mathbf{u}(x, y, z) \approx \mathbf{U}_{KJL}(x, y, z), \quad (3.21)$$

the partial differential equation

$$\frac{\partial \mathbf{u}}{\partial t} = f_T(\mathbf{u}), \quad (3.22)$$

becomes an extremely large set of ODEs

$$\frac{d\mathbf{U}_{KJL}}{dt} = F_T(\mathbf{U}_{KJL}), \quad (3.23)$$

where  $f_T(\mathbf{u})$  is the forward time evolution operator of the Navier-Stokes equation, and  $F_T(\mathbf{U}_{KJL})$  is its spectral approximation via (3.6). The temporal ODE can be

solved in any number of ways – `Channelflow` allows the user to choose from several implicit-explicit methods,<sup>2</sup>: Crank-Nicolson Forward Euler, Crank-Nicolson Adams-Basforth, Spalart-Moser Runge-Kutta and Semi-implicit Backwards Differentiation of orders 1 to 4. The order 3 Semi-implicit Backwards Differentiation (SBDF3) was chosen by default, and no reason to change this was anticipated, since SBDF3 is known to allow relatively large time steps while maintaining low error for moderate-to-large  $Re$  [29].

## 3.2 Newton-Krylov-Hookstep Method

In order to find exact coherent structures it is necessary to solve the equation

$$\mathbf{u} - \sigma f_T(\mathbf{u}) = \mathcal{R}_T(\mathbf{u}) = 0, \quad (3.24)$$

which is most easily tackled by root-finding algorithms. The root finding method used by `Channelflow` is based on Newton's method with some additional refinements, which are discussed below.

### 3.2.1 Newton's Method

The principle behind Newton's method is as follows: Suppose  $f(x)$  is a smooth and differentiable function and that we have a ‘good’ initial guess  $x_0$  for one of its roots. How good a guess needs to be is highly dependent on the problem. For this thesis, an initial condition that gave  $\mathcal{R}_T(\mathbf{u}) < 0.001$  was considered a sufficiently good guess. Then we can find a better guess for the root of  $f$  by finding the root of the tangent line at  $f(x_0)$ , as shown in Figure 3.1. Mathematically, this is given by

$$f(x_n) + f'(x_n)(x_{n+1} - x_n) = 0, \quad (3.25)$$

So that

$$x_{n+1} = x_n - \frac{f(x_n)}{f'(x_n)}, \quad (3.26)$$

where  $x_n$  is the  $n$ -th guess for the root. In higher dimensions, (3.25–3.26) are replaced by the matrix equations

$$\mathbf{f}(\mathbf{x}_n) + \mathbb{J}_{f,\mathbf{x}_n}(\mathbf{x}_{n+1} - \mathbf{x}_n) = 0, \quad (3.27)$$

$$\mathbf{x}_{n+1} = \mathbf{x}_n - \mathbb{J}_{f,\mathbf{x}_n}^{-1} \mathbf{f}(\mathbf{x}_n), \quad (3.28)$$

where  $\mathbb{J}_{f,\mathbf{x}_n}$  is the Jacobian of  $\mathbf{f}$  evaluated at  $\mathbf{x}_n$ .

---

<sup>2</sup>The implicit part is used to solve the nonlinear, convective acceleration term of the Navier-Stokes equations, and the explicit part is used on the linear terms.

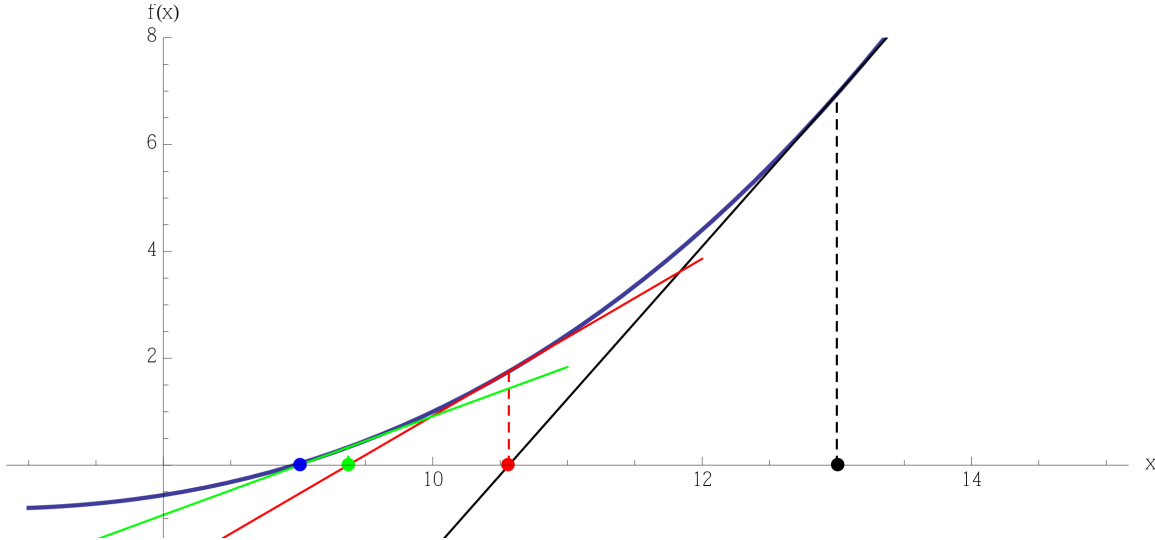


Figure 3.1: A demonstration of Newton’s method in 1D on a simple function with the root at  $x_r \approx 8.98$ . Starting at  $x_0 = 13$ , the first tangent (black) has a zero at  $x_1 \approx 10.5$ , the second tangent (red) has a zero at  $x_2 \approx 9.4$ , and the third tangent (green) has a zero at  $x_3 \approx 8.99$ . The method converges to within approximately  $10^{-4}$  in just three steps.

Newton’s method is extremely fast and converges quadratically on the root [30], but is not guaranteed to do so - a simple example is if the  $n$ -th guess is at (or very close to) a local minimum, in which case the second term of (3.26) will explode, taking us very far away from the initial, good guess, as in Figure 3.2. Furthermore, in a system with around  $10^5$  unknowns, inverting the Jacobian (or for that matter, calculating the Jacobian) in (3.27) becomes very time consuming. To offset the inversion timing issue (we will deal with actually calculating the Jacobian later), we can trade off accuracy for speed by replacing (3.27) with a minimization problem

$$\|\mathbf{f}(\mathbf{x}_n) + \mathbb{J}_{\mathbf{f}, \mathbf{x}_n} \mathbf{d}\mathbf{x}_n\| = r_n < \epsilon \|\mathbf{f}(\mathbf{x}_n)\|, \quad (3.29)$$

where  $\|\mathbf{x}\| = \sqrt{\mathbf{x} \cdot \mathbf{x}}$  is the norm of  $\mathbf{x}$ ,  $r_n$  is the residual at the  $n$ -th iteration,  $\mathbf{d}\mathbf{x}_n = \mathbf{x}_{n+1} - \mathbf{x}_n$  and  $\epsilon$  is some small parameter that controls how accurate we want the minimization to be [31]. Note that if  $\epsilon = 0$ , we recover (3.27). Newton’s method can be terminated either when successive steps fail to refine  $\mathbf{x}_n$  sufficiently, or when  $f(\mathbf{x})$  is sufficiently small.

### 3.2.2 The Generalized Minimum Residual Method

There are a vast quantity of residual minimization algorithms in existence, each typically optimized for a particular class of problem. **Channelflow** uses the **Generalized Minimum RESidual** (GMRES) method, a Krylov subspace method developed in 1986 by Saad and Schultz [32]. To illustrate the principle of GMRES, consider the least squares problem of finding the  $\mathbf{x} \in \mathbb{R}^n$  that minimizes

$$\|\mathbf{Ax} - \mathbf{b}\| = r, \quad (3.30)$$

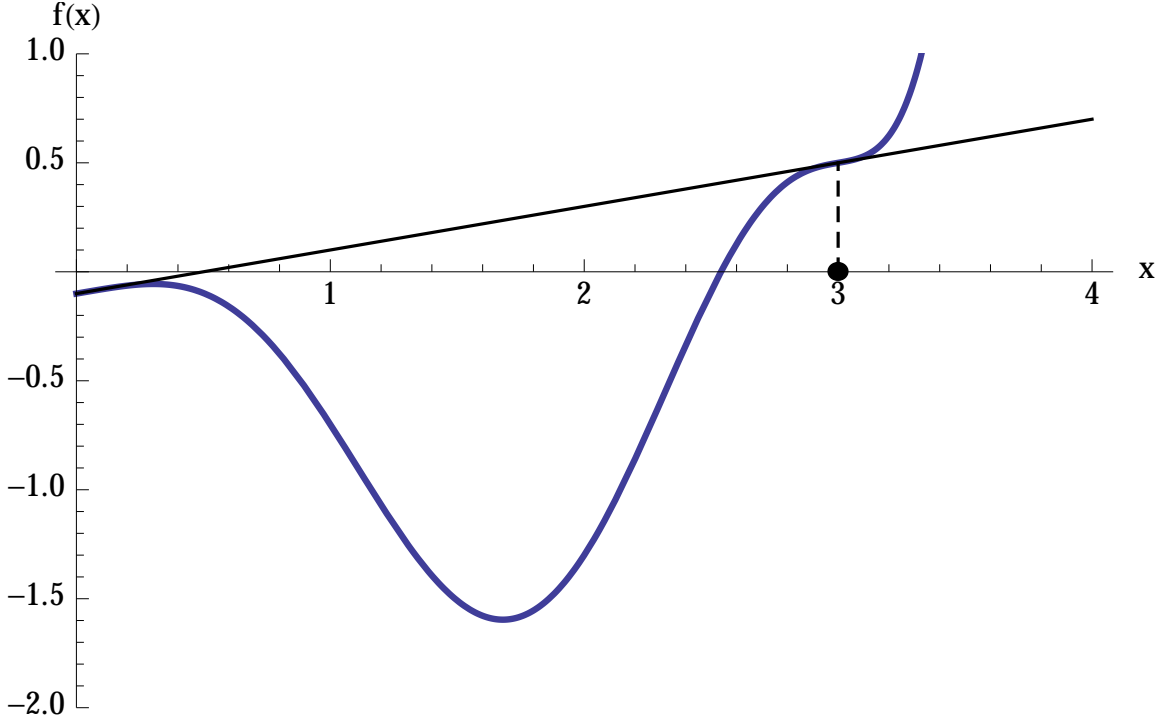


Figure 3.2: If we assume the linear model remains valid for the entire step, we can sometimes be led astray. Because the function is linear only in the vicinity of the initial guess, the Newton step takes us very far away from the actual root we are trying to find, and will likely never converge.

where  $\mathbb{A} \in \mathbb{R}^{n \times n}$  and  $\mathbf{b} \in \mathbb{R}^n$ . The similarity of (3.30) to (3.29) makes the formulation of a solution to (3.30) vital.

### 3.2.2.1 The Krylov Subspace

Since (3.30) is a model problem for (3.29), let  $n \sim O(10^5)$ . A search in such a huge space would be extremely time consuming, so instead the GMRES method searches for a vector  $\mathbf{x}$  in a drastically lower dimensional **Krylov subspace**. The  $k$ -th Krylov subspace for (3.30) with a guess  $\mathbf{x}_0$  is defined

$$\mathcal{K}_k(\mathbb{A}, \mathbf{b} - \mathbb{A}\mathbf{x}_0) = \text{span} (\mathbf{b} - \mathbb{A}\mathbf{x}_0, \mathbb{A}(\mathbf{b} - \mathbb{A}\mathbf{x}_0), \mathbb{A}^2(\mathbf{b} - \mathbb{A}\mathbf{x}_0) \dots, \mathbb{A}^{k-1}(\mathbf{b} - \mathbb{A}\mathbf{x}_0)), \quad (3.31)$$

### 3.2.2.2 The Arnoldi Iteration

As mentioned earlier, both the calculation and inversion of the  $\mathbb{A}$  are extremely difficult, precluding the use of (3.31) to generate the Krylov subspace. The Krylov subspace is therefore generated via Algorithm 1, which is known as the **Arnoldi Iteration** [33].

**Algorithm 1.** Begin with  $\mathbf{q}_1 = \mathbf{b} - \mathbb{A}\mathbf{x}_0$ . Then for the  $k$ -th Arnoldi iteration,

1. calculate  $h_{ik} = \mathbb{A}\mathbf{q}_i \cdot \mathbf{q}_k$ , for  $i = 1, 2, \dots, k$ ,
2. generate  $\mathbf{p} = \mathbb{A}\mathbf{q}_k - \sum_{i=1}^k h_{ik}\mathbf{q}_i$ ,
3. calculate  $h_{k+1,k} = \|\mathbf{p}\|$ ,
4. and normalize  $\mathbf{q}_{k+1} = \frac{\mathbf{p}}{h_{k+1,k}}$

Note something absolutely vital to the Arnoldi iteration - at **no point** in the iteration is an explicit calculation of  $\mathbb{A}$  necessary, since it always appears as a matrix-vector product! Thus, we resolve the issue of calculating what will, in the case of **Channelflow**, be the  $10^5$  by  $10^5$  Jacobian matrix. Incidentally, the Arnoldi iteration can in general be used to solve the eigenvalue problem for a matrix,<sup>3</sup> which will prove to be useful later.

### 3.2.2.3 GMRES Strikes Back

If we let  $\mathbb{Q}_k = [\mathbf{q}_1 | \mathbf{q}_2 | \dots | \mathbf{q}_k]$  and define  $\mathbb{Q}_k^\dagger$  as the **conjugate transpose** of  $\mathbb{Q}_k$  then

$$\mathbb{H}_k = \mathbb{Q}_k^\dagger \mathbb{A} \mathbb{Q}_k, \quad (3.32)$$

and

$$\mathbb{A} \mathbb{Q}_k = \mathbb{Q}_{k+1} \tilde{\mathbb{H}}_k, \quad (3.33)$$

where  $\tilde{\mathbb{H}}_k$  is  $\mathbb{H}_k$  with an additional row  $[0, 0, 0, \dots, h_{k+1,k}]$ . Following the derivation in [34], if  $\mathbf{z} \in \mathcal{K}_k(\mathbb{A}, \mathbf{b} - \mathbb{A}\mathbf{x}_0)$ ,

$$\mathbf{z} = \mathbb{Q}_k \mathbf{y}, \quad (3.34)$$

for some  $\mathbf{y}$ . Then

$$\begin{aligned} \mathbb{A} \mathbf{z} &= \mathbb{A} \mathbb{Q}_k \mathbf{y}, \\ &= \mathbb{Q}_{k+1} \tilde{\mathbb{H}}_k \mathbf{y}, \end{aligned} \quad (3.35)$$

so by restricting our guess to the Krylov subspace, (3.30) can be written as

$$\|\mathbb{Q}_{k+1} \tilde{\mathbb{H}}_k \mathbf{y} - (\mathbf{b} - \mathbb{A}\mathbf{x}_0)\| = r. \quad (3.36)$$

Since multiplication by a unitary matrix<sup>4</sup> does not affect the norm, and  $\mathbb{Q}_k$  is, by construction, unitary, (3.36) becomes

$$\|\mathbb{Q}_{k+1}^\dagger \mathbb{Q}_{k+1} \tilde{\mathbb{H}}_k \mathbf{y} - \mathbb{Q}_{k+1}^\dagger (\mathbf{b} - \mathbb{A}\mathbf{x}_0)\| = r, \quad (3.37)$$

$$\|\tilde{\mathbb{H}}_k \mathbf{y} - \mathbb{Q}_{k+1}^\dagger (\mathbf{b} - \mathbb{A}\mathbf{x}_0)\| = r. \quad (3.38)$$

---

<sup>3</sup>That is, solving for the eigenvectors  $\mathbf{q}_k$  and eigenvalues  $\lambda_k$  that satisfy  $\mathbb{A}\mathbf{q}_k = \lambda_k\mathbf{q}_k$

<sup>4</sup>That is, conjugate transpose is its inverse.

The second term of the norm is a vector of the form

$$\mathbb{Q}_{k+1}^\dagger (\mathbf{b} - \mathbb{A}\mathbf{x}_0) = \begin{pmatrix} \mathbf{q}_1^\dagger(\mathbf{b} - \mathbb{A}\mathbf{x}_0) \\ \mathbf{q}_2^\dagger(\mathbf{b} - \mathbb{A}\mathbf{x}_0) \\ \vdots \\ \mathbf{q}_{k+1}^\dagger(\mathbf{b} - \mathbb{A}\mathbf{x}_0) \end{pmatrix}, \quad (3.39)$$

but since, from the definition of the Krylov subspace,  $\mathbb{Q}_1 = \text{span}(\mathbf{b} - \mathbb{A}\mathbf{x}_0) = [\mathbf{q}_1]$ ,

$$\mathbf{q}_1 = \frac{\mathbf{b} - \mathbb{A}\mathbf{x}_0}{\|\mathbf{b} - \mathbb{A}\mathbf{x}_0\|}. \quad (3.40)$$

Since the Arnoldi iteration naturally produces an orthonormal set of  $\mathbf{q}_i$ , (3.39) simplifies to

$$\mathbb{Q}_{k+1}^*(\mathbf{b} - \mathbb{A}\mathbf{x}_0) = \begin{pmatrix} \|\mathbf{b} - \mathbb{A}\mathbf{x}_0\| \\ 0 \\ \vdots \\ 0 \end{pmatrix} = \|\mathbf{b} - \mathbb{A}\mathbf{x}_0\| \begin{pmatrix} 1 \\ 0 \\ \vdots \\ 0 \end{pmatrix} = \|\mathbf{b} - \mathbb{A}\mathbf{x}_0\| \mathbf{e}_1. \quad (3.41)$$

Substituting this into (3.37) provides the final residual problem

$$\left\| \|\mathbf{b} - \mathbb{A}\mathbf{x}_0\| \mathbf{e}_1 - \tilde{\mathbb{H}}_k \mathbf{y} \right\| = r, \quad (3.42)$$

that is solved by Algorithm 2.

**Algorithm 2.** Begin with

$$\begin{aligned} \mathbf{c} &= \mathbf{b} - \mathbb{A}\mathbf{x}_0, \\ \mathbf{q}_1 &= \frac{\mathbf{c}}{\|\mathbf{c}\|}, \\ \mathbb{Q}_1 &= [\mathbf{q}_1], \\ \mathcal{K}_1(\mathbb{A}, \mathbf{c}) &= \text{span}(\mathbf{q}_1). \end{aligned}$$

Then the  $k$ -th GMRES iteration is given by

1. generating  $\mathbf{q}_{k+1}$ ,  $\mathbb{Q}_{k+1}$  and  $\tilde{\mathbb{H}}_k$  via the Arnoldi iteration,
2. finding the  $\mathbf{y}_{k+1}$  that minimizes (3.42),
3. and computing  $\mathbf{x}_{k+1} = \mathbb{Q}_{k+1} \mathbf{y}_{k+1}$ .

The second step of Algorithm 2 may seem nonsensical - why have we put this much effort into getting an equation similar to (3.30)? The key lies in realizing that the minimization problem in Algorithm 2 has a dimension of  $k$ , whereas (3.30) has a dimension on the order of  $10^5$ . Since the matrix inversion problem scales as dimension to the third power, this reduction is extremely powerful – especially since GMRES converges quickly – in this thesis, GMRES rarely took more than 20 iterations to converge. The minimization step in Algorithm 2 can be solved via a QR decomposition, which has a time complexity of  $O(n)$  [35].

### 3.2.3 The Hookstep

While Newton's method is incredibly powerful, it needs to be provided a sufficiently good guess to stand a chance of converging to a solution. However, in practice, we are limited in our ability to provide good guesses by our computational resources, since we are searching for the proverbial needle in a  $10^5$  dimensional haystack. As a consequence, even our best guesses may be less than ideal for a pure Newton method – for example, the linear model used in deriving Newton's method may not be valid for the Newton step  $\mathbf{dx}_N$ , as shown in Figure 3.2.

If this is the case, switching to a constrained **hookstep** can force the algorithm to take artificially smaller steps, until the linear model becomes locally accurate. In `Channelflow`, the equation of constraint for the hookstep  $\mathbf{dx}_H$  is

$$\|\mathbf{dx}_H\| \leq \delta, \quad (3.43)$$

where  $\delta$  is known as the **trust region** of the local linear model – that is, the region around the guess where the function remains approximately linear. The hookstep is further restricted to lie in the  $k$ -th Krylov subspace, so that

$$\mathbf{dx}_H = \mathbb{Q}_k \mathbf{s}, \quad (3.44)$$

where  $\mathbf{s}$  is now the  $k$ -dimensional step that we need to take. As with the Newton step, the hookstep is determined using GMRES. Unlike the Newton step, the minimization stage of Algorithm 2 is not computed via the QR decomposition [19]. Instead, we substitute (3.33) and (3.44) into (3.30), giving the residual which we wish to minimize with respect to  $\mathbf{s}$ ,

$$\|\mathbb{Q}_{k+1}^T \mathbf{b} - \tilde{\mathbb{H}}_k \mathbf{s}\| = r. \quad (3.45)$$

Applying the singular value decomposition,<sup>5</sup>  $\tilde{\mathbb{H}}_k = \mathbb{U} \mathbb{D} \mathbb{V}^T$  transforms (3.45) into

$$\|\hat{\mathbf{b}} - \mathbb{D} \hat{\mathbf{s}}\| = r, \quad (3.46)$$

where  $\hat{\mathbf{s}} = \mathbb{V}^T \mathbf{s}$ ,  $\hat{\mathbf{b}} = \mathbb{U}^T \mathbb{Q}_{k+1}^T \mathbf{b}$ . Using Lagrange multipliers, the minimization problem in Algorithm 2 yields the solution [19]

$$\hat{s}_i = \frac{\hat{b}_i D_{ii}}{D_{ii}^2 + \mu}, \quad (3.47)$$

where  $\mu$  minimizes

$$\|\hat{\mathbf{s}}(\mu)\|^2 - \delta^2 = \tau, \quad (3.48)$$

which can be trivially solved by a 1D Newton method.

---

<sup>5</sup>The singular value decomposition is a method by which a matrix  $\mathbb{A} \in \mathbb{R}^{n \times m}$  is factorized into the product  $\mathbb{U} \mathbb{D} \mathbb{V}^T$ , where  $\mathbb{U} \in \mathbb{R}^{n \times n}$  and  $\mathbb{V} \in \mathbb{R}^{m \times m}$  are unitary matrices, and  $\mathbb{D} \in \mathbb{R}^{n \times m}$  is a diagonal matrix.

### 3.3 Recurrence Diagrams

While the augmentation of the Newton-Krylov method by the hookstep makes it more resilient against poor guesses, the Newton-Krylov-Hookstep (NKH) method remains extremely sensitive to initial conditions. As a result, a method to generate decent guesses to kickstart the NKH solver is vital. One way to do this is to try to find some underlying pattern in a trajectory that could hint at the presence of exact coherent structures. For example, we could view the trajectory in the dissipation and energy input plane, as in [15], which has proven successful in the past. Generalizing this method, we can consider the **recurrence diagram** of the trajectory, which can be generated via Algorithm 3.

**Algorithm 3.**

1. Begin with an initial condition. This can be chosen by randomly generating a velocity field, or making a slight random perturbation off of a known exact coherent structure.
2. Integrate this initial condition forward in time using SBDF3 to obtain a trajectory.
3. Calculate some metric of the trajectory that provides insight into its dynamical structure.
4. Extract some number of good guesses from this metric, and pass them along to the NKH solver.

In particular, calculating the metric

$$\mathfrak{R}(t, T) = \|\mathbf{u}(t + T) - \mathbf{u}(t)\|, \quad (3.49)$$

where  $\mathfrak{R}(t, T)$ , measures the distance of the field at time  $t + T$  from the field at time  $t$ . When using this metric, the recurrence diagram naturally becomes a method by which the separation in state space of successive flow states in a trajectory can be visually and numerically analyzed, since small values of  $\mathfrak{R}$  indicate points in the  $(t, T)$  plane where the state space separation of the fields is also small. Interpretation of a recurrence diagram is not an exact science - for example, a naive search for the minimum of Figure 3.3 would yield all the points for which  $T = 0$ . Experience has shown that long, horizontal streaks of low values correspond to the shadowing of a periodic orbit, and tend to be excellent sources of good guesses for the NKH solver.<sup>6</sup>

However, (3.49) is only useful for exact coherent structures with no relative velocity, and thus can only be applied when neither spanwise nor streamwise symmetry is broken. To deal with the case when streamwise or spanwise symmetry is broken, we

---

<sup>6</sup>From John Gibson, private communication.

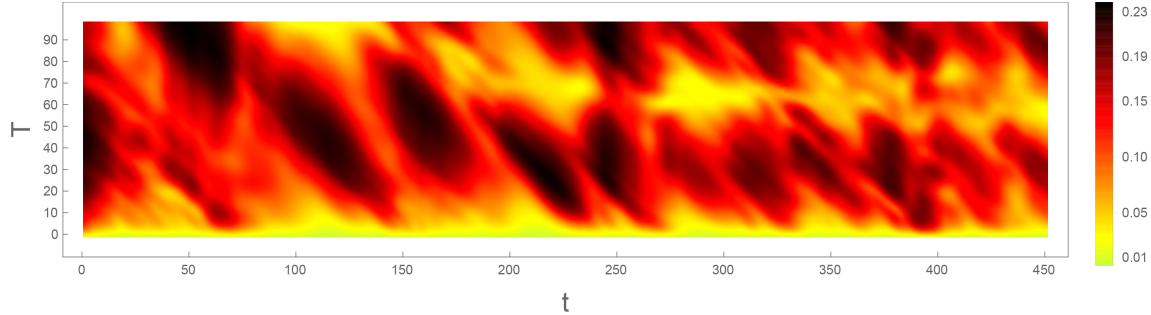


Figure 3.3: A recurrence plot which was used to find one of the new periodic orbits (P60) presented in this thesis. At each point, the value of  $\mathfrak{R}(t, T) = \|\mathbf{u}(t+T) - \mathbf{u}(t)\|$  is plotted. Light colorations correspond to low values, and vice versa. Notice the long, thin streak of low values from  $t = 200$  to  $t = 450$  for  $T \approx 60$ . A guess sourced from this band was the initial guess that led to the discovery of P60.

modified (3.49) to allow for the possibility of relative equilibria or periodic orbits, by changing the problem to finding small values of

$$\mathfrak{R}(t, T, l_x, l_z) = \|\tau(l_x, l_z)\mathbf{u}(t+T) - \mathbf{u}(t)\|. \quad (3.50)$$

This is now a 3 or 4 dimensional minimization problem, since we now need to find low values of  $\mathfrak{R}$  in the recurrence domain  $[0, t_{\max}] \times [0, T_{\max}] \times [l_x, \min, l_x, \max] \times [l_z, \min, l_z, \max]$ . The most obvious consequence of the increase in the dimension of the minimization domain is that the time complexity of calculating  $\mathfrak{R}$  increases from  $O(n^2)$  to up to  $O(n^4)$ . A more fundamental issue, however, is that the visual approach to analyzing recurrence diagrams now appears unusable, since visualizing a 4D domain is not practical. We sidestep the issue by developing and using Algorithm 4. Algorithm 4 works by finding the phase shift that minimizes the residual for a given  $(t, T)$ , and saves only that value of the residual, thus reducing the dimension of the recurrence diagram back to 2 dimensions. Unfortunately, Algorithm 4 does nothing to offset the significant increase in calculations needed to fully calculate the recurrence diagram. However, a glance at Figure 3.3 shows that a large part of the diagram contains no patterns at all, and is functionally useless. For this reason, when looking for solutions with broken symmetry, the initial recurrence diagram is computed at a significantly lower resolution than it would have been for a trajectory in the fully symmetric space. When features are identified in the low resolution recurrence diagram, we can construct a higher resolution diagram around the features that are worthy of further consideration. This method reduces the time required to find good guesses from several days to a single day, or less. The workflow detailed above is summarized in Figure 3.4.

**Algorithm 4.** For a trajectory  $\mathbf{u}(t)$  with a recurrence domain  $[t_0, t'] \times [0, T_{\max}] \times [l_x, \min, l_x, \max] \times [l_z, \min, l_z, \max]$ ,

1. for a  $(t, T) \in [t_0, t'] \times [0, T_{\max}]$ ,
2. find  $\mathfrak{R}(t, T, l_x, l_z)$  for each  $(l_x, l_z) \in [l_x, \min, l_x, \max] \times [l_z, \min, l_z, \max]$  and

3. save only the smallest  $\mathfrak{R}$  and the minimizing  $(l_x, l_z)$  found this way,  
 for each  $(t, T) \in [t_0, t'] \times [0, T_{\max}]$ .

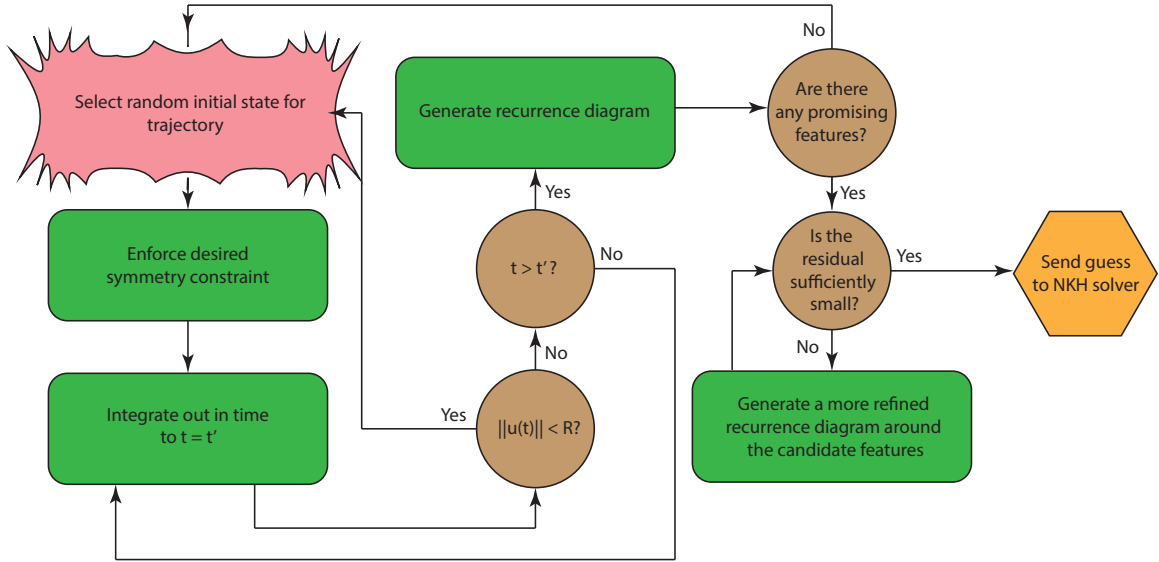


Figure 3.4: A flow chart that lays out the procedure used to find exact coherent structures. We begin by selecting a random initial state for the trajectory. This initial state can either be found by generating a truly random state, or by applying a small, random perturbation to known exact coherent structures. The desired symmetry constraints are then enforced, and the trajectory is integrated from  $t = 0$  to  $t = t'$ . After every time step, if the state's norm has dropped below some threshold  $R$  (I use 0.1), we assume that the trajectory has relaminarized, and find a new initial condition to work with. Once the integration is over, we generate the recurrence diagram according to (3.49), for some  $T_{\max}$ , and attempt to find any patterns that we would associate with exact coherent structures. If no patterns are found, we find another initial state and repeat the process. If there are some candidate patterns, we calculate the minimum  $\mathfrak{R}$  of that feature. If it is below about  $10^{-4}$ , we accept it as a potential solution, and pass it to the NKH solver. If  $\mathfrak{R}$  is not low enough, it is likely not a sufficiently good guess to cause the NKH solver to converge in a reasonable time, so we zoom in on the pattern and calculate a refined recurrence graph, until either the minimum value of the pattern is low enough, or it becomes apparent that the pattern is unlikely to produce a meaningful initial guess

### 3.4 Parametric Continuation

If we have a solution to (3.24) for some control parameters, such as  $Re$  or the cell size, we may wish to see how these solutions vary with these control parameters. For example, if we know that a solution  $S$  exists for  $Re = 400$ , we might want to know how this solution differs from the solution  $S'$  at  $Re = 200$ , assuming that  $S'$  exists. The solution may, for example vary as in Figure 3.5, and new solutions may appear, disappear, or vary in stability in **bifurcations**. Finding bifurcations can be extremely helpful in understanding the behaviour. One of the most efficient ways to find these solutions is via Algorithm 5, which is known as **parametric continuation**.

**Algorithm 5.** If we have a solution  $S_{\mu_0}$  with a control parameter  $\mu_0$ , and a solution finding method  $\mathfrak{S}(S, \mu)$ , then  $S_{\mu_k}$  can be found by

1. choosing a  $\mu_{i+1} = \mu_i + d\mu$  such that the residual  $\mathfrak{S}(S_{\mu_i}, \mu_{i+1})$  is small,
2. and then using  $S_{\mu_i}$  as a guess for  $\mathfrak{S}$  to find  $S_{\mu_{i+1}}$ ,

for  $i = 1, 2, \dots, k - 1$ .

At this point, the underlying numerical framework has been laid bare to the point that it is at the very least, a slightly gray box. Applying the methods of the previous chapters took a great deal of trial and error,<sup>7</sup> but has nevertheless proven successful. In the following chapter, I will present four new periodic orbits that I discovered for plane Couette flow and discuss their properties.

---

<sup>7</sup>Mostly the latter.

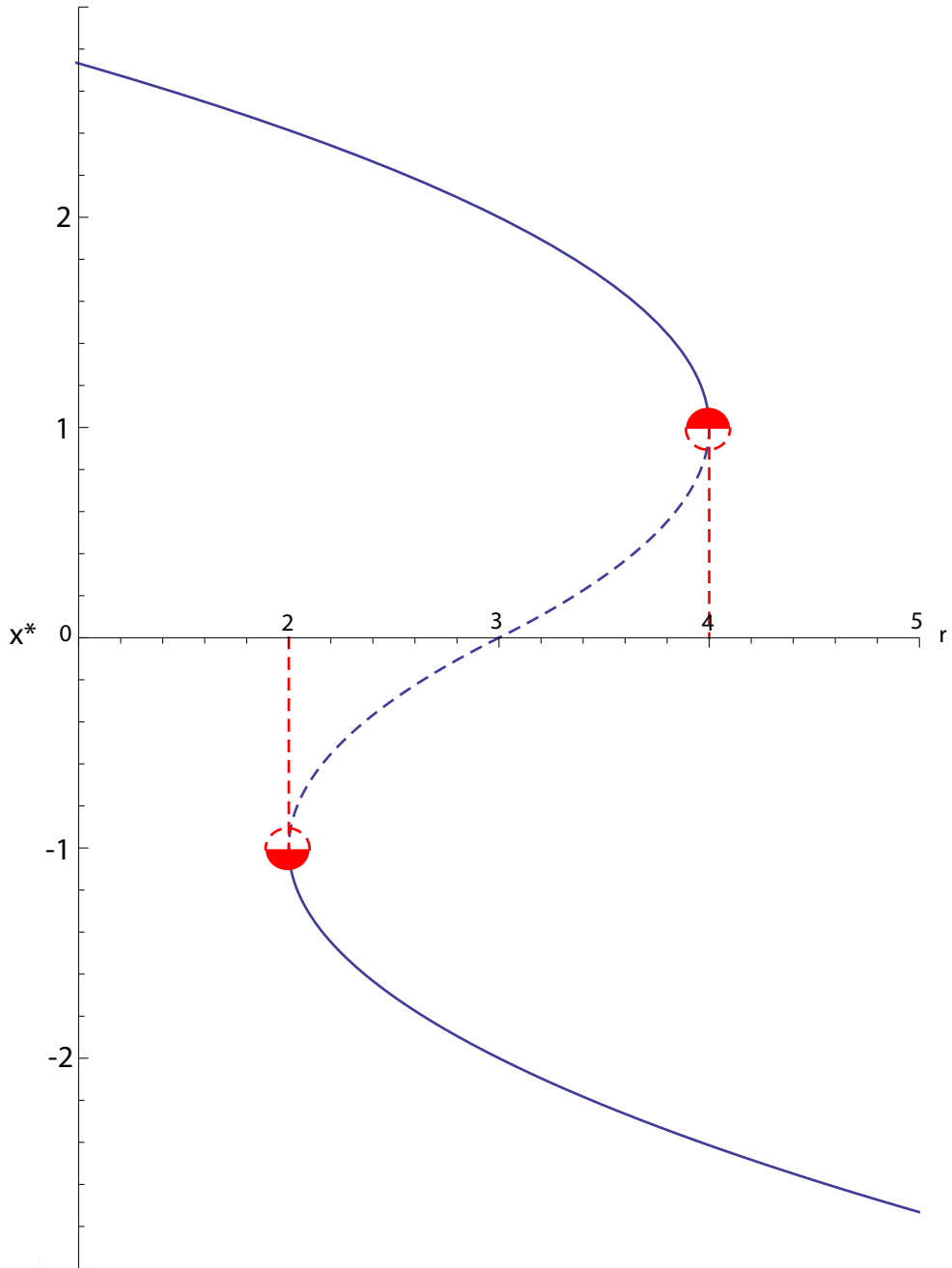


Figure 3.5: A schematic of a 1D bifurcation, that shows the variation of a solution  $x^*$  such that  $f(x^*) = 0$  as a function of a control parameter  $r$ . While the control parameter  $r < 2$ , there is only one, stable solution, on the left. At a critical value  $r = 2$ , however, a new solution emerges at  $x^* = -1$  in a **saddle-node bifurcation**. While  $2 < r < 4$ , the saddle-node splits into two, producing a stable lower solution (solid), and an unstable upper solution (dashed). As  $r$  approaches 4, the original stable solution and the new unstable solution approach each other until at  $r = 4$ , they annihilate in another saddle node bifurcation, leaving only the new stable solution. In higher dimensions, bifurcations can be incredibly complex, but we can nevertheless observe bifurcations of this form.



# Chapter 4

## Results

The first law of thermodynamics  
says that work cannot be destroyed.  
We who use computers know better.

---

A frustrated Ph.D. candidate

### 4.1 The Gang of Four

Four new periodic orbits P85, P60, P32 and P8 (Figures 4.1, 4.2, 4.3 and 4.4), also known as the Gang of Four, have been found, with properties that are summarized in Table 4.1. I was unable to find any exact coherent structures in the fully unconstrained phase space.

Table 4.1: A summary of relevant information regarding the Gang of Four. All of these results are presented at  $Re = 400$ , in the Hamilton-Kim-Waleffe cell [36] with  $(L_x, L_z) = (5.51157, 3.76239)$ , and grid discretization  $(N_x, N_y, N_z) = (48, 33, 48)$ . The label for each orbit is based on its period, which experience shows uniquely defines an orbit. The phase velocities  $v_x$  and  $v_z$  are in terms of fraction of cell length per period. The largest Floquet exponent and number of unstable Floquet exponents are explained in a later section, as are the mean dissipation and energy input. The symmetry isotropy subgroup of each orbit is also provided.

Label	$T$	$v_x$	$v_z$	$\lambda_{\max}$	# $\lambda_{\text{unstable}}$	$\bar{D}/\bar{I}$	Symmetry
P85	85.50	0	0	0.0427	6	1.85	S
P60	60.86	0	0	0.032749	10	2.08	S
P32	32.00	0.5	0	$0.0200 + 0.0982i$	7	1.98	$S_x$
P8	8.32	0	$2.29 \times 10^{-7}$	$0.0998 - 0.2605i$	20	4.00	$S_z$

### 4.1.1 Visualizations

Visualizing the behavior of fluids is in itself a time-honored discipline, especially when CFD is involved,<sup>1</sup> and well chosen visualization schemes can be, in and of themselves, an excellent tool for interpreting and analyzing data. Here, we use two main visualization methods.

#### 4.1.1.1 Orthographic Projection

Figures 4.1, 4.2, 4.3 and 4.4 are all examples of the first visualization method – the **orthographic projection** (OP) [18]. The OP is constructed by piecing together several representative 2D slices of the state’s velocity field – each of the periodic boundaries, and the mid-plane, and is colored to represent the magnitude and direction of streamwise velocity. The OP allows us to visually interrogate the structure of the state, which can be extremely useful – for example, it is clear purely from visual interrogation that Figure 4.4 is less ordered than Figure 4.1. However, the OP cannot deliver much more than this – for example, it cannot easily tell us much about the differences between the orbits of, say, P8 and P85. For this reason, we use the second, more useful visualization method - the state space projection [18].

#### 4.1.1.2 State Space Projection

If we have a set of  $k$  basis vectors  $\mathbf{q}_i$  that are orthonormal and span a subspace  $\mathfrak{V}_k \subset \mathfrak{V}$  of dimension  $k$ , then the projection of a vector  $\mathbf{v} \in \mathfrak{V}$  onto  $\mathfrak{V}_k$  is defined

$$\mathbf{v}_k = \sum_{i=1}^k c_i \mathbf{q}_i, \quad (4.1)$$

where  $c_i = \mathbf{v} \cdot \mathbf{q}_i$ . When  $k$  is either 2 or 3, we can visualize the  $n$ -dimensional trajectory as a 2 or 3 dimensional trajectory instead. While we lose information in making this projection, we can still gain a great deal of valuable information about trajectories. Projecting the four periodic orbits in Figures 4.1 through 4.4 onto a basis constructed from orthonormalizing the initial conditions of each orbit results in the state space projection in Figure 4.5.

The main issue with the state space projection method, however, is that a state must be **congruent** to a basis to be projected onto it - that is, both the box length and grid discretization must be the same for both the state and the projection basis. Many previous investigations [5, 18] have important results in the W03 cell, where  $(L_x, L_z) = (5.51157, 2.51327)$ , with corresponding state space projections. In order to compare to these results, I attempted to use Algorithm 5 to continue the four periodic orbits into the W03 cell, which leads me to the next important result.

---

<sup>1</sup>As the old joke goes, CFD really stands for **C**olorful **F**luid **D**ynamics.

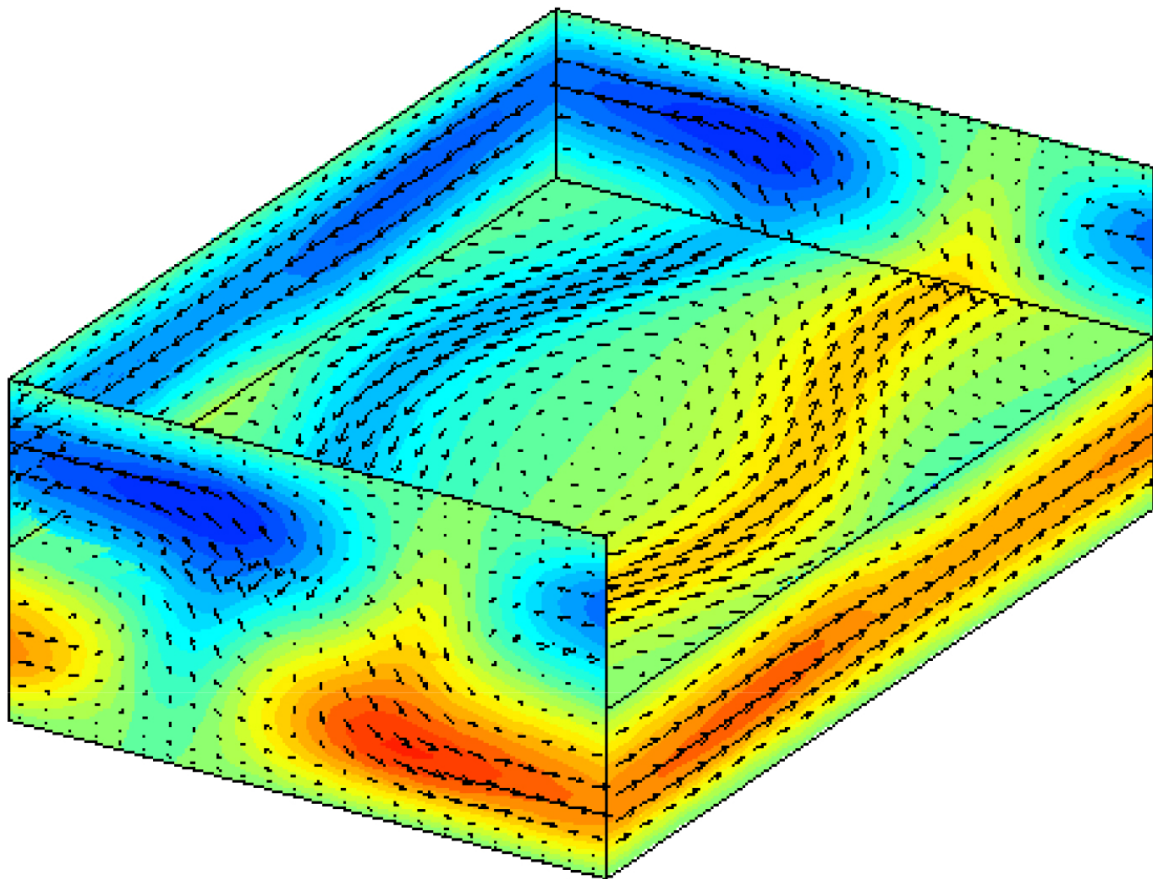


Figure 4.1: OP of P85. P85 is a fully symmetric orbit with period 85.50 in the HKW cell at  $Re = 400$ . Note the extreme symmetry of the prominent streaks visible in the mid-plane. The velocity field pictured here is the turbulent perturbation only; the laminar flow has been subtracted away. Available at <https://youtu.be/r6ac1b54vDk>

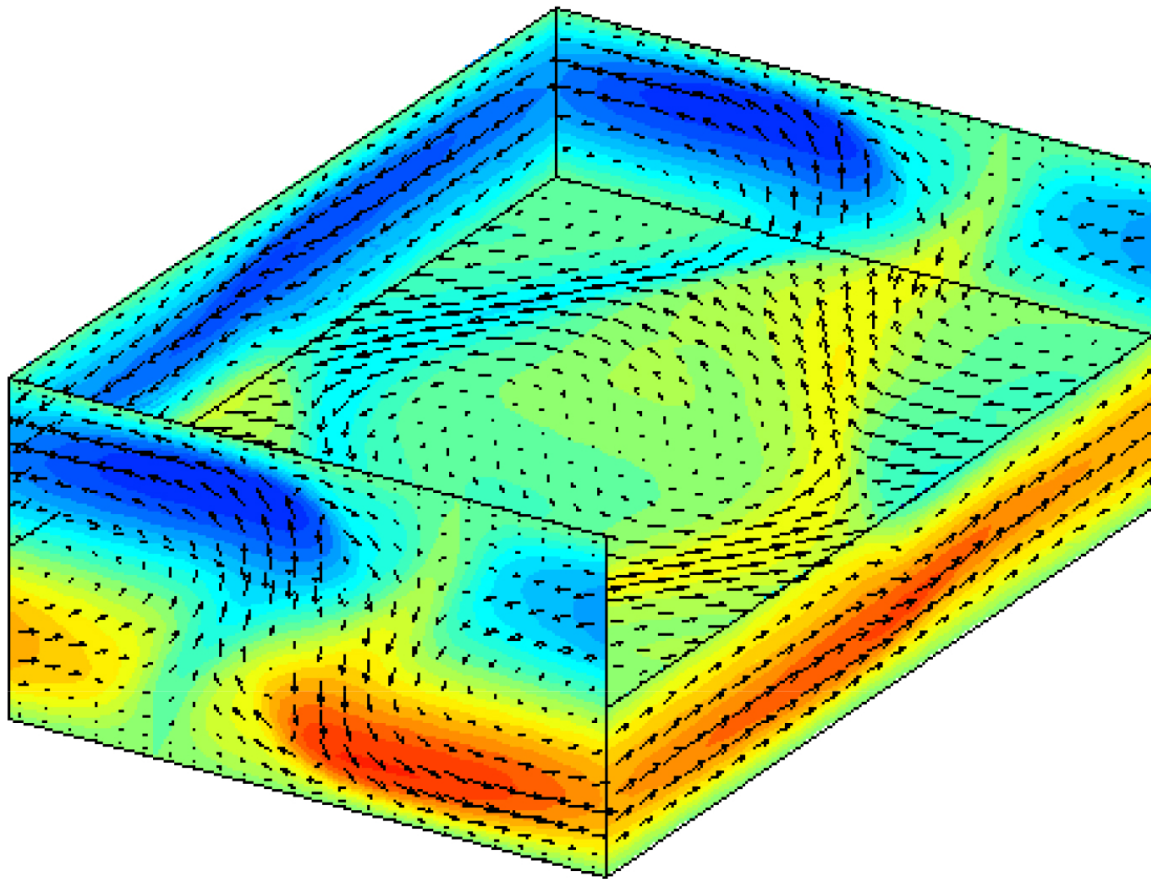


Figure 4.2: OP of P60. P60 is another fully symmetric orbit with period 60.86 in the HKW cell with  $Re = 400$ . While it displays an ellipsoid streak structure similar to P85, the energy of these streaks is lower. The velocity field pictured here is the turbulent perturbation only; the laminar flow has been subtracted away. Available at <https://www.youtube.com/watch?v=ulyMrSfxW5U>

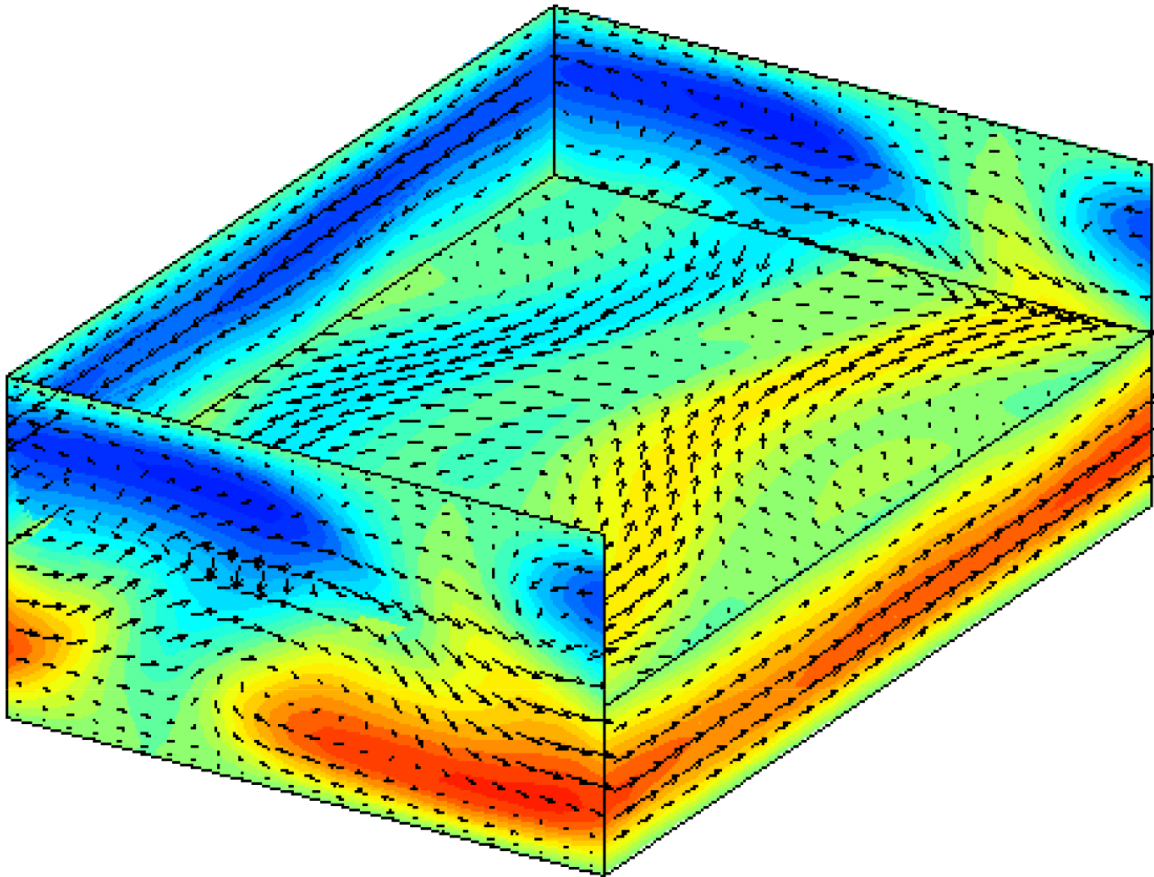


Figure 4.3: OP of P32. P32 is a streamwise asymmetric periodic orbit fixed by the symmetry group  $S_z$ , which is functionally a mirror symmetry about the streamwise axis. However, notice that while P32 does not *exactly* maintain rotational symmetry about the streamwise axis, it bears remarkable similarity to P85 and P60. The rotational symmetry residual was  $10^{-3}$ , which is a few orders of magnitude lower than symmetries that are obviously not satisfied, but is not low enough ( $10^{-6}$ ) to be accepted as a legitimate symmetry. In the HKW cell at  $Re = 400$ , the period is 32.00, and the streamwise relative velocity is  $-0.5$  cell lengths per period. The velocity field pictured here is the turbulent perturbation only; the laminar flow has been subtracted away. Available at <https://www.youtube.com/watch?v=qDGBxX50bKY>

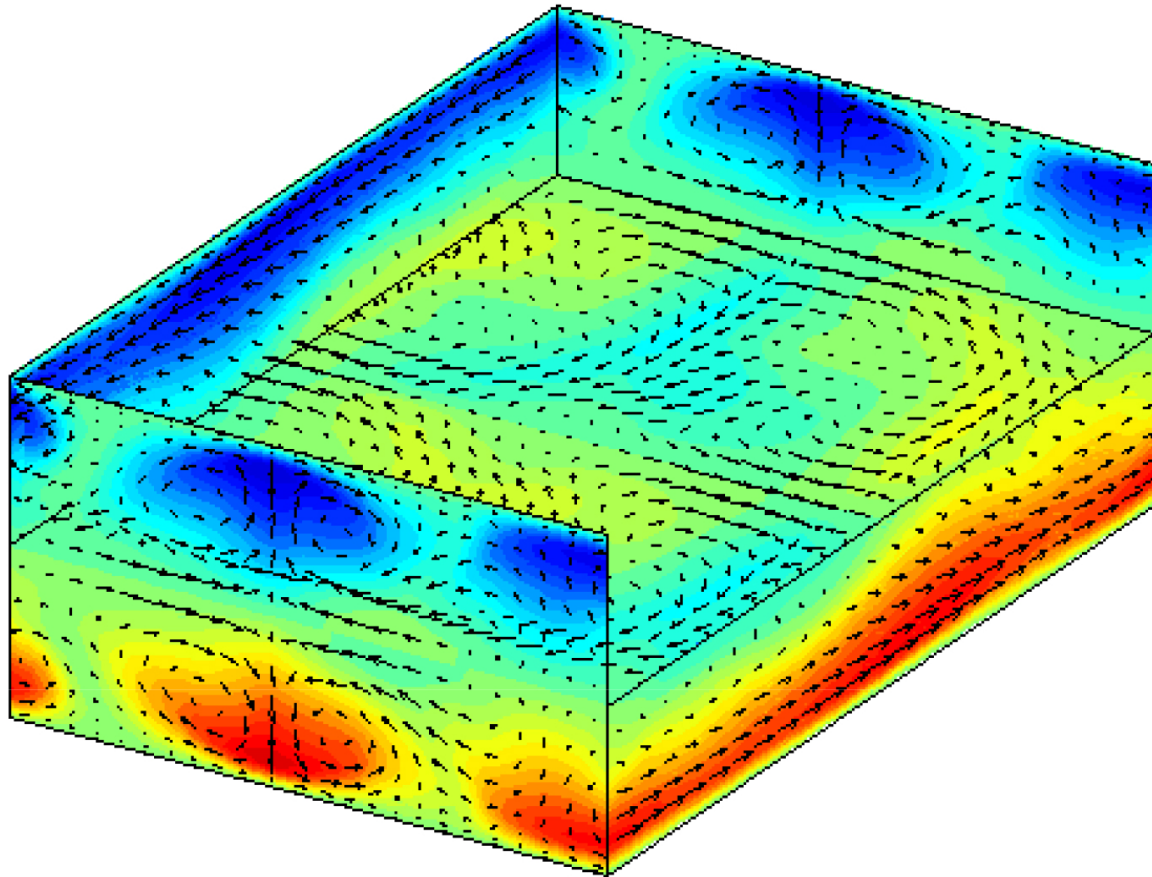


Figure 4.4: OP of P8. P8 is a spanwise asymmetric periodic orbit fixed by the symmetry group  $S_x$ , which is functionally a rotation by  $\pi$  about the spanwise axis. In the HKW cell at  $Re = 400$ , the period is 8.32, and the spanwise relative velocity is  $2.29 \times 10^{-7}$  cell lengths per period. This number may seem low, but if it is not accounted for, the NKH solver cannot converge. P8 also has a rather short period, almost an order of magnitude shorter than most orbits recorded in the database at [channelflow.org](http://channelflow.org). Since the Arnoldi iteration has a time cost that scales linearly with the period, P8 has been the least computationally demanding period orbit to analyze. The velocity field pictured here is the turbulent perturbation only; the laminar flow has been subtracted away. Available at <https://youtu.be/-ad0U55T39w>

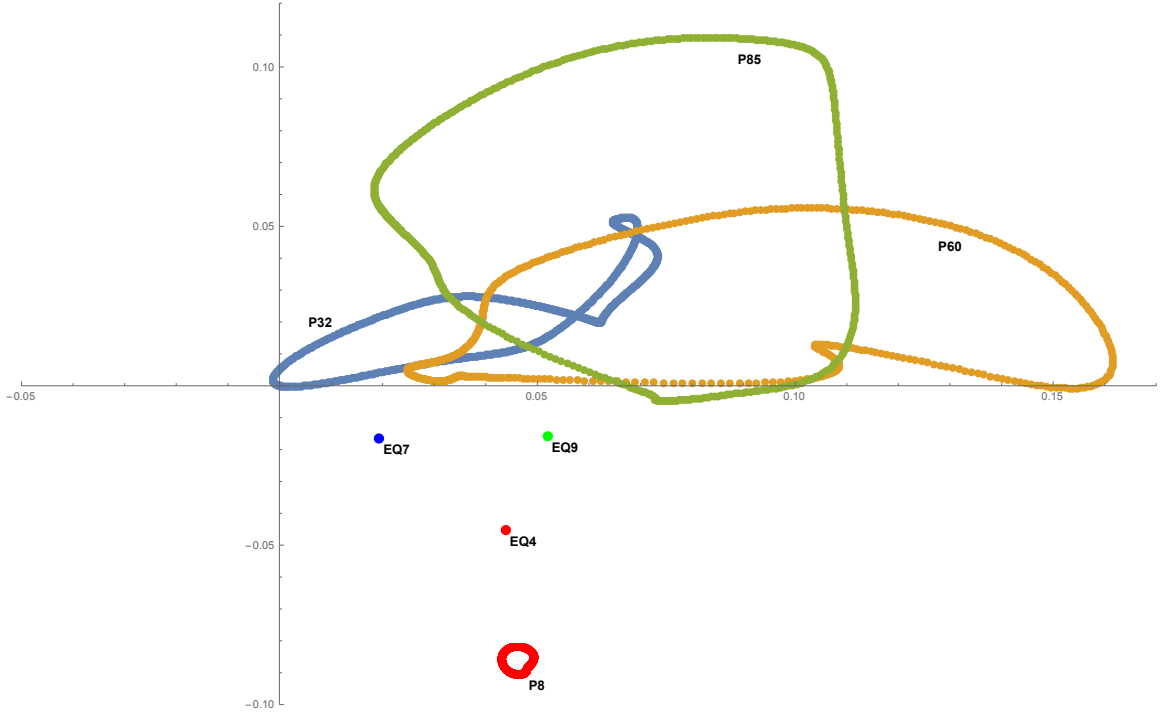


Figure 4.5: 2D state space projection of the Gang of Four and some reference equilibria. The basis vectors for the projection were constructed by orthonormalizing the initial states of each of the periodic orbits. This results in a 4D state space projection, of which we can take 2D slices (of which there are 6), or 3D slices (of which there are 4). The equilibria are fully symmetric, and were found by Halcrow [5]. Notice that the P8 orbit is separated by the equilibria from P85, P60 and P32, a feature that holds true in the other 5 2D projections.

## 4.2 Spanwise Continuation

When Algorithm 5 was used to continue P8 down to the W03 cell, the data presented in Figure 4.6 was produced. Initially, the continuation algorithm decreases  $L_z$  and increases  $T$ , but at  $L_z \approx 2.8$ , the algorithm reverses itself, decreasing  $T$  and increasing  $L_z$ , until  $L_z \approx 2.95$ , when the algorithm resumes decreasing  $L_z$  and increasing  $T$ . Since we expect that the period of an orbit ought to uniquely define the orbit,<sup>2</sup> the existence of multiple, distinct orbits for  $2.8 \leq L_z \leq 2.96$  hints at a bifurcation. The similarity of Figure 4.6 to Figure 3.5 is striking, and led me to suspect the possibility that P8 undergoes some form of bifurcation at  $L_z \approx 2.8$  and  $L_z \approx 2.95$ . However, Algorithm 5 relaxes the convergence criteria to  $10^{-10}$  to speed

<sup>2</sup>We generally assume that if two solutions have differing periods, they are distinct, which may seem reasonable - but holes in such a simple criterion are evident almost immediately. For example, two ‘distinct’ orbits with periods  $T_1$  and  $T_2$  may in fact be the same orbit, with period  $|T_2 - T_1|$ , that has simply repeated more times for one orbit than for the other. This hole can be plugged by any number of methods, most easiest by simply calculating  $\|\mathbf{u}_1(t) - \mathbf{u}_2\|$  over the entire period. If the norm is never small, then the orbits are distinct.

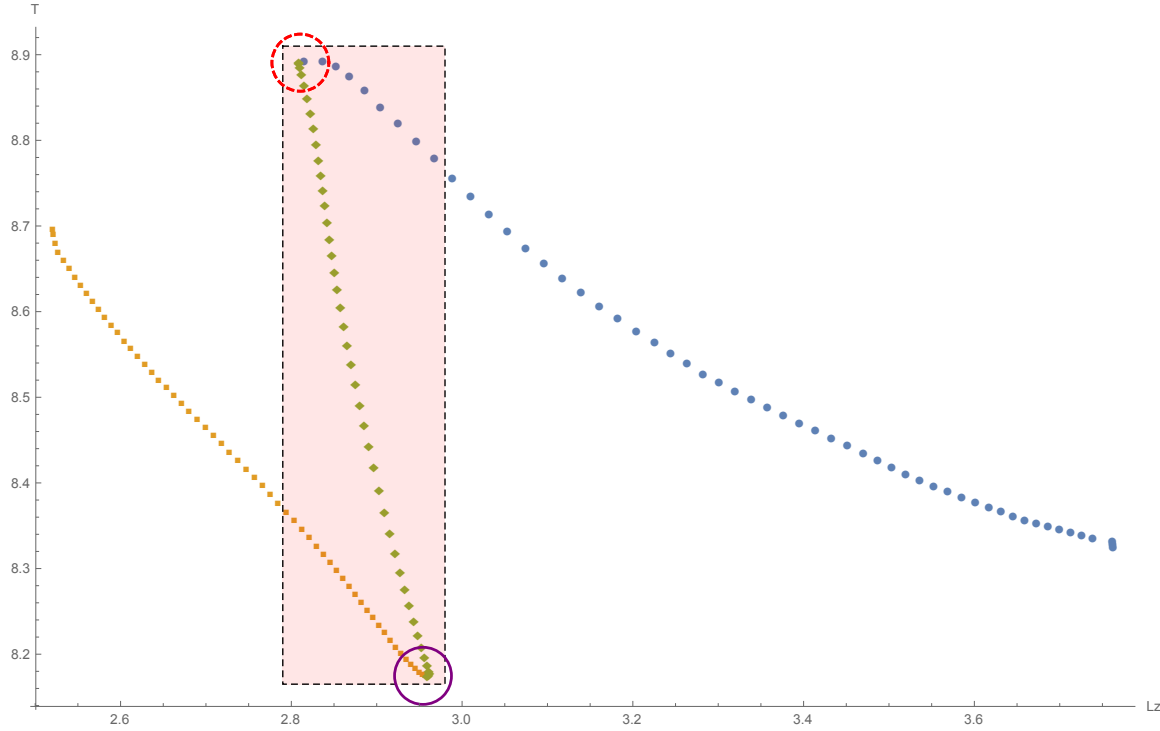


Figure 4.6: Period as a function of spanwise cell length for P8. The data can be sectioned into three distinct parts. First, the **upper branch** (blue circles), which is the path that the continuation algorithm initially follows in parameter space. Second, the **transition branch** (green diamonds), which occurs after the **first turning point** (red, dashed circle). Third, the **lower branch** (orange rectangles), after the **second turning point** (purple, solid circle). Within the marked rectangular region, multiple distinct solutions exist for the same cell length, hinting at a bifurcation. Searches with higher resolution have pinned down the turning points to the interval  $L_z \in [2.8087, 2.8096]$  for the first turning point, and  $L_z \in [2.6150, 2.6157]$  for the second turning point.

up the parametric continuation process, and as a result, may have found artificial solutions, so I verified the existence of multiple distinct solutions for  $L_z = 2.925$  and  $(N_x, N_y, N_z) = (62, 53, 62)$  to  $10^{-13}$ . It is important to note that this in and of itself does not necessarily prove that a bifurcation exists – for example, the continuation algorithm may have simply found *another* periodic orbit’s trajectory and hopped onto that. When a bifurcation occurs, the qualitative behavior of solutions pre and post-bifurcation tend to be markedly different. For low-dimensional systems, this is easy to evaluate, since one can visually identify changes in the phase space, as in Figure 4.7. For higher-dimensional systems, such an approach is not feasible.

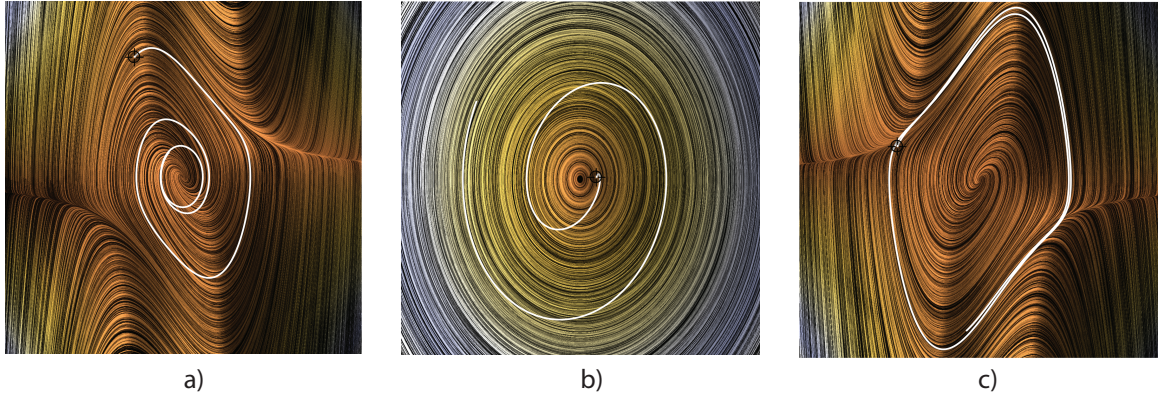


Figure 4.7: Phase portrait of the Van Der Pol oscillator and its Hopf bifurcation, with trajectories in white. (a), for negative values of the bifurcation parameter, the single periodic orbit is unstable, so an initial condition that begins near the orbit spirals away from it. (b), when the bifurcation parameter is zero, there is no periodic orbit. (c), for positive values of the bifurcation parameter, the periodic orbit is stable, and initial conditions are attracted into the orbit.

### 4.2.1 Linear Stability Analysis

We can instead turn to **linear stability analysis**. If  $\mathbf{u}$  is a periodic orbit with period  $T$ , then for a small perturbation  $d\mathbf{u}$ ,

$$f_T(\mathbf{u} + d\mathbf{u}) - \mathbf{u} = f_T(\mathbf{u}) - \mathbf{u} + \mathbb{J}_{T,\mathbf{u}}d\mathbf{u} = \mathbb{J}_{T,\mathbf{u}}d\mathbf{u}, \quad (4.2)$$

where  $\mathbb{J}_{T,\mathbf{u}}$  is the Jacobian of the Navier-Stokes forward-time map evaluated at  $\mathbf{u}$ . The stability of the orbit is determined by how  $d\mathbf{u}$  changes over time - if it shrinks, then the orbit is stable, but if it grows, it is unstable. Writing  $d\mathbf{u}$  as a linear combination of the eigenvectors  $\mathbf{v}_i$  of  $\mathbb{J}_{T,\mathbf{u}}$ , the right-hand side of (4.2) becomes

$$\mathbb{J}_{T,\mathbf{u}}d\mathbf{u} = \mathbb{J}_{T,\mathbf{u}} \sum_{i=1}^n c_i \mathbf{v}_i = \sum_{i=1}^n c_i \lambda_i \mathbf{v}_i, \quad (4.3)$$

where the  $\lambda_i$  are the corresponding eigenvalues, known as the **Floquet exponents**, whose real parts measure the exponential rate of decay or growth of the corresponding eigenvector.<sup>3</sup> From this definition, it is clear that the periodic orbit can only be stable against infinitesimal perturbations if  $\text{Re}[\lambda_i] \leq 0 \ \forall i$ , and unstable otherwise. The eigenvalues for the Navier-Stokes forward-time map can be calculated by Algorithm 1. The eigenvalues of P8 in the HKW cell at  $Re = 400$  are shown in Figure 4.8

In general, we would expect that as the control parameter changes, the Lyapunov exponents would also. In particular, if a change in the control parameter resulted in the Lyapunov exponent changing sign, the qualitative behavior of the periodic orbit would change, resulting in a bifurcation. Applying the Arnoldi iteration to the states near the turning points of Figure 4.6 results in Figure 4.9 and Figure 4.10.

<sup>3</sup>The real parts are known as the **Lyapunov exponents**. The imaginary part contributes only to the oscillatory behavior.

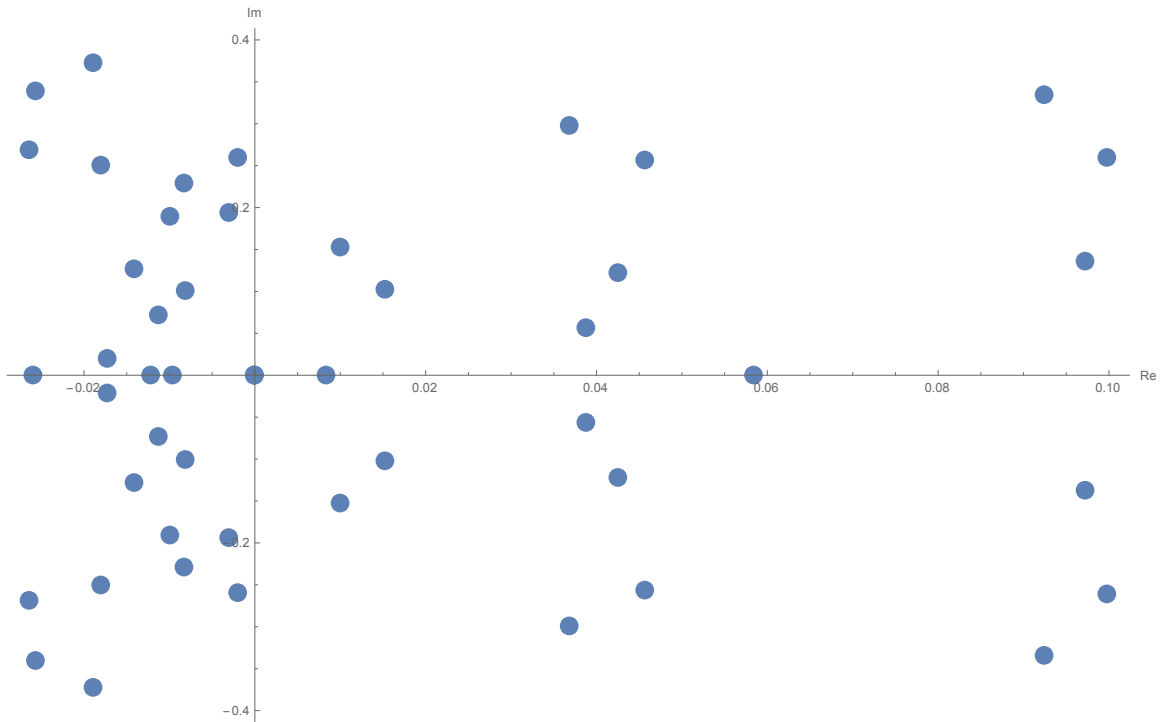


Figure 4.8: All 20 unstable eigenvalues, and the 80 largest stable or marginal ( $|\lambda| \ll 1$ ) eigenvalues of P8, in the HKW cell at  $Re = 400$ . Note that the eigenvalues come in conjugate pairs. Since there are eigenvalues with positive real parts, the periodic orbit is unstable, as expected. Note that since the Jacobian likely has full rank, and likely also has no repeating nonzero eigenvalues, there are several orders of magnitude more stable eigenvalues than there are unstable. Since the Arnoldi iteration will find the larger eigenvalues first, all the unstable eigenvalues are shown, whereas only the weakly stable eigenvalues are calculated.

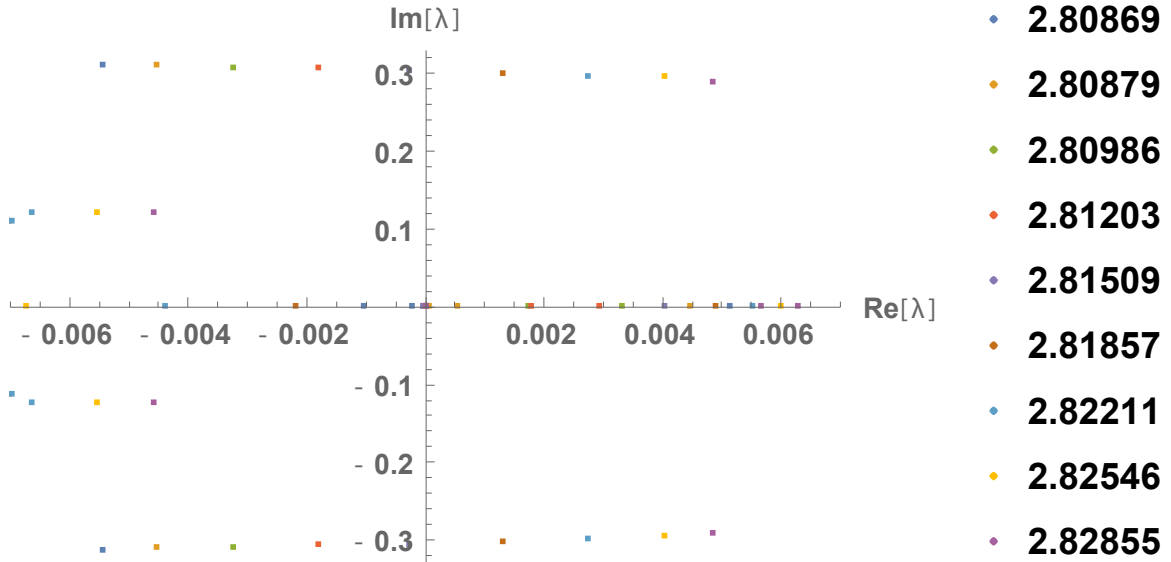


Figure 4.9: Eigenvalues of  $P_8$  as a function of  $L_z$  at the first turning point. When the real part of the eigenvalue switches sign, the associated eigenvector switches stability. Therefore, the line of eigenvalues with imaginary part  $\approx \pm 0.3$  are of special interest. The real part of the eigenvalue likely switches sign at some  $L_z \in [2.81509, 2.81857]$ , compared to the first turning point, which likely occurs for  $L_z \in [2.8087205, 2.8096095]$ .

Figures 4.9 and 4.10 have a set of eigenvalues that switch sign at  $L_z$  values that are reasonably consistent with turning point data from Figure 4.6. It therefore seems likely that these turning points do in fact correspond to bifurcations. Qualitative differences between the upper and transition branch are also apparent from observations of movies of the periodic orbit.<sup>4</sup> From the video, it appears that the upper branch has more energy concentrated in the streaks than the transition branch, which in turn appears to have more energy in the mid-plane.

### 4.2.2 Return of the State Space

Having used linear stability analysis to find the unstable eigenvector, we can use the state space projection to visualize the effect of a slight perturbation, as in Figure 4.11. Here, we see the effect of a slight perturbation along the most unstable eigenvector  $P8E1$ , with eigenvalue  $0.0998 - 0.2605i$ . Now Figure 4.11 is noisy, and difficult to analyze. To deal with this, we can construct the **Poincare section** of a trajectory. The Poincaré section of a  $k$  dimensional trajectory is constructed by keeping track of where the trajectory crosses a  $k - 1$  dimensional surface. The Poincaré section for  $P8E1$ , displayed in Figure 4.12 displays the qualitative behavior we would expect for a complex eigenvalue - the real part is negative and the perturbation grows, the

<sup>4</sup> Available at <https://youtu.be/JDzQfjx5Cmg>

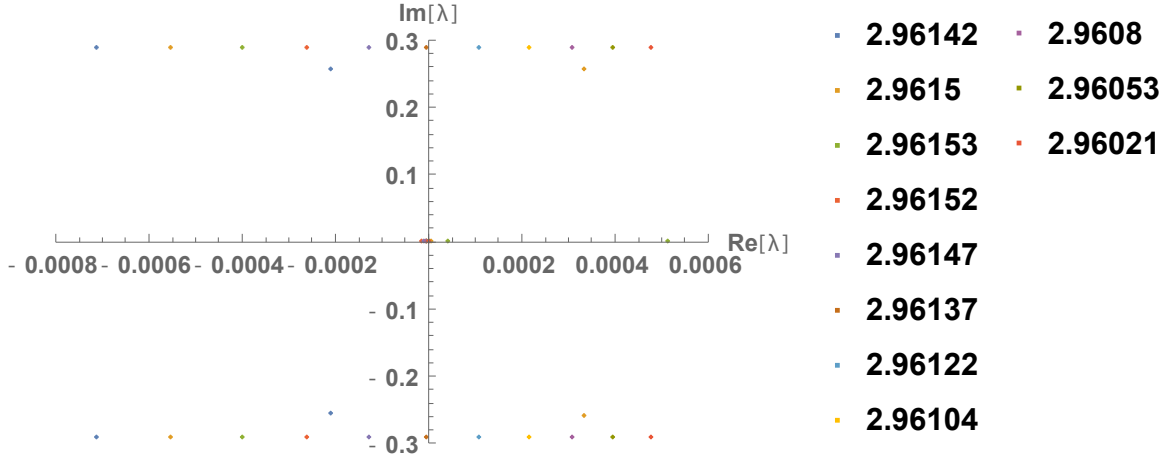


Figure 4.10: Eigenvalues of P8 as a function of  $L_z$  at the second turning point. Here, two sets of eigenvalues have real parts that switch signs, first in the interval  $L_z \in [2.96122, 2.96137]$  and second in the interval  $L_z \in [2.96142, 2.9615]$ . The second stability switch is consistent with the position of the second turning point, which occurs in the interval  $L_z \in [2.6150, 2.6157]$ .

imaginary part is nonzero, and the perturbation spirals around the initial position. Even though the eigenvalue is only valid locally, we can still see that it approximately predicts the behavior of the trajectory - from the imaginary part of the eigenvalue, we can see that it ought to take approximately 25 time units for a full rotation in the Poincare section. Figure 4.12 suggests that approximately 5 orbits have taken place for a full rotation in the Poincare section, each with periods that are approximately 8 time units. This does not agree exactly,<sup>5</sup> but one must remember that the Floquet exponents are a *local* model of the orbit, and naturally become less precise the more the perturbation grows.<sup>6</sup>

## 4.3 Dissipation and Energy Input

### 4.3.1 A New Projection

While Figure 4.5 seems to indicate that P8 is a special member of the Gang of Four – an assertion which is backed up by the marked difference in the properties displayed in Table 4.1 – the striking dissimilarity in Figure 4.5 may be an artifact of the projection basis. To address this issue, we can also project onto the **dissipation-energy input**

<sup>5</sup>Or very well at all, especially since we've just come from having residuals on the order of  $10^{-14}$

<sup>6</sup>As a matter of fact, the pictured spiral is the last spiral the Poincare section trajectory executes, though the trajectory in the full space continues to look qualitatively similar to the original orbit for a long time.

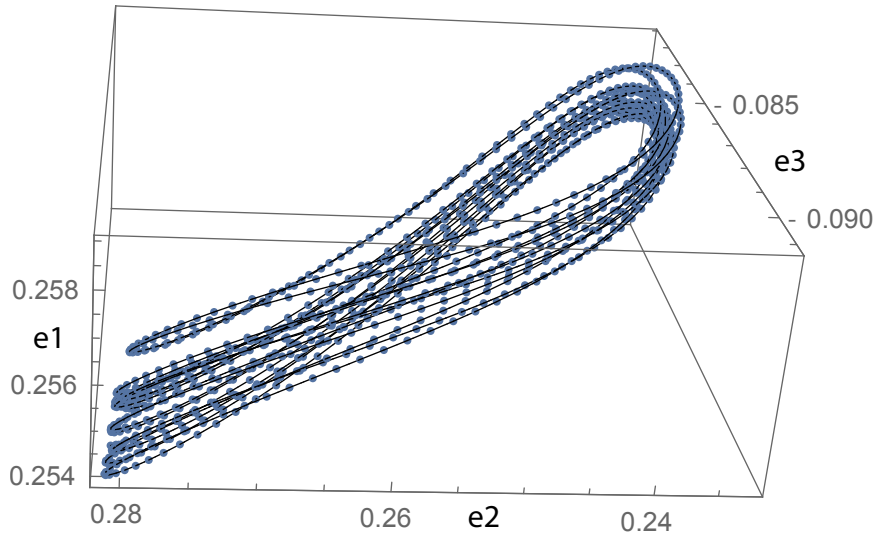


Figure 4.11: The trajectory of a slight perturbation along the most unstable eigenvector, projected onto a difference slice of the same basis as in Figure 4.5. Notice that it keeps the general shape of the orbit that spawned it, at least for short time spans.

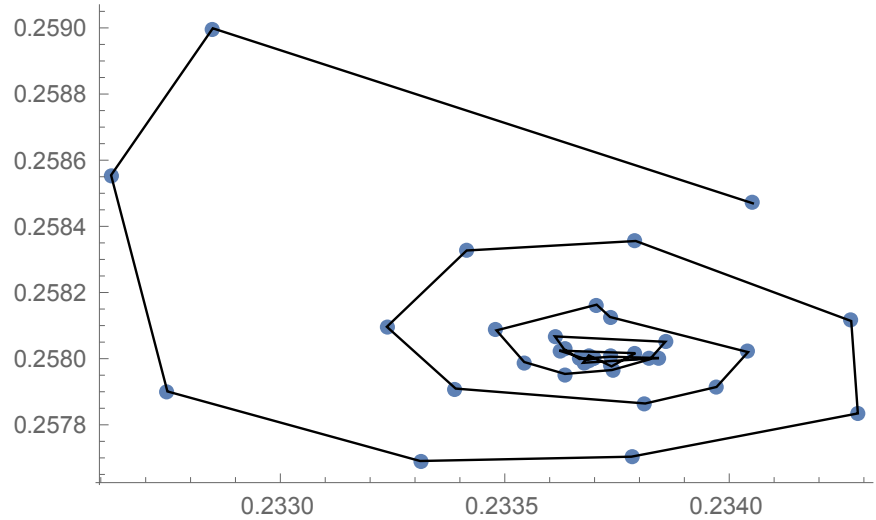


Figure 4.12: Poincaré section of Figure 4.11, defined by the surface  $e_2 = 0.26$ . Notice that the trajectory along the Poincaré section spirals outwards, as we would expect for an unstable manifold with a complex eigenvalue.

plane, where the dissipation  $D$  and energy input  $I$  are defined

$$D(t) = \frac{1}{L_x L_y L_z} \int_0^{L_x} \int_0^{L_y} \int_0^{L_z} |\nabla \times \mathbf{u}(t)|^2 dz dy dx, \quad (4.4)$$

$$I(t) = 1 + \frac{1}{2L_x L_z} \int_0^{L_x} \int_0^{L_z} \left. \frac{\partial \mathbf{u}_y}{\partial y} \right|_{y=1} + \left. \frac{\partial \mathbf{u}_y}{\partial y} \right|_{y=-1} dz dx. \quad (4.5)$$

Unlike the state space projection, which is to some extent an artificial projection mechanism, the dissipation-input energy plane projection has real physical meaning, and thus is a more natural projection. Applying (4.4–4.5) to the Gang of Four results in Figure 4.13,<sup>7</sup> which suggests that the distinctive features of P8 are likely not artificial. However, a glance at Figure 4.14, which overlays random turbulent trajectories on Figure 4.13 suggests that P8 is the only member of the Gang of Four that does not seem to directly influence turbulent trajectories in any significant way, and that P85 may have a significant influence instead. However, since the Arnoldi iteration scales linearly with the period, analysis of any of the longer orbits would take an unfeasibly long time with my computing resources. As a result, I will continue to limit my analysis to P8.<sup>8</sup>

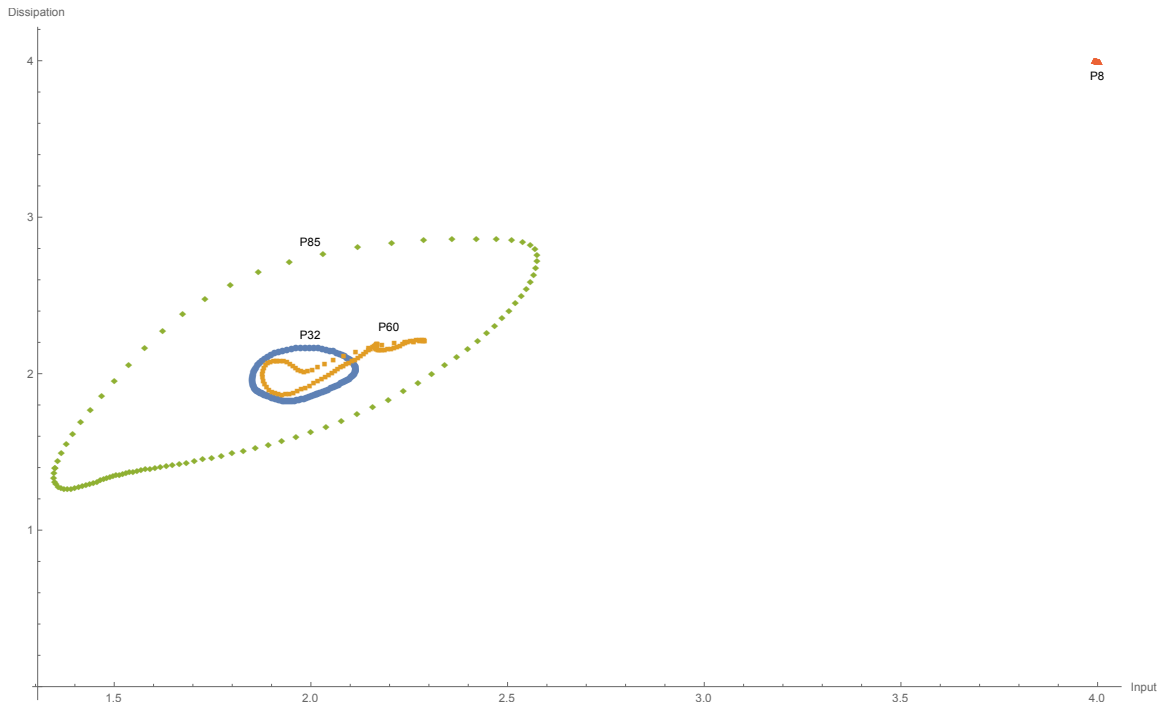


Figure 4.13: Dissipation versus energy input for the Gang of Four. While the lesser members of the Gang remain clustered towards a input/dissipation of 2, P8 stays at a dissipation/input of 4. Due to P8’s low period, the fine details of its orbit cannot be discerned here. The separation observed in Figure 4.5 is clearly reflected in this physically important projection.

<sup>7</sup>Note that for a periodic orbit, the mean dissipation and energy input need to be balanced, which explains why all observed solutions do not stray far away from the line  $D(I) = I$ .

<sup>8</sup>For example, a single iteration of Algorithm 5 takes about 2 hours for P8, which allowed me to collect the data presented in Figure 4.6 in about a week. The same process would have taken more than a month for P32, and several for P60 and P85.

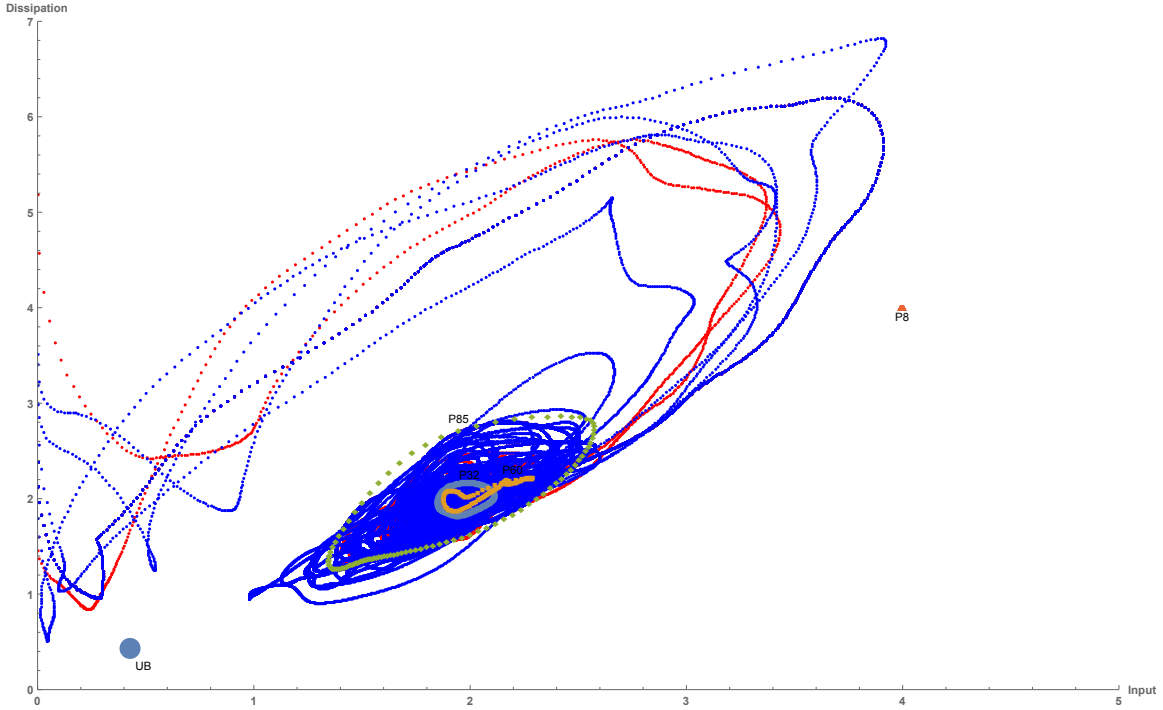


Figure 4.14: Dissipation versus energy input for 20 turbulent trajectories (red and blue) beginning from random initial conditions, with perturbations of magnitude 0.3 overlaid on the Gang of Four and the Nagata upper branch equilibrium. The data implies that P8 contributes very little to the dynamics of turbulence, since turbulent trajectories do not appear to ‘live’ near P8. It does, however, suggest that P85 may have some importance in turbulent transition, since the trajectories only remain‘bound’ to a narrow area of D-I space while they are within the orbit of P85.

### 4.3.2 The Search for Bifurcations, Part II

The dissipation-energy input projection has another extremely important benefit – it is domain-agnostic. This allows us to compare the different branches of Figure 4.6 in a more sophisticated manner. Since the full bifurcation diagram spans a vast distance in the dissipation-energy input plane, the projection is divided into three parts, with the upper branch in Figure 4.15, the transition branch in Figure 4.16 and the lower branch in Figure 4.17, where the divisions between branches is informed by Figure 4.6. Unfortunately, apart from the expected repulsion of the upper branch from the high dissipation/energy input zone, nothing particularly interesting occurs here.

However, a glance at Figures 4.15, 4.16 and 4.17 indicates that they are by and large elliptical in shape, so the area enclosed by the orbit can easily be calculated by the singular value decomposition. Applying this method and ordering by traversal down the continuation trajectory gives Figure 4.18, whereas ordering by  $L_z$  gives Figure 4.19. The results of this analysis are promising, since they show structural changes in a physically important projection, which occur near the expected location

## Dissipation

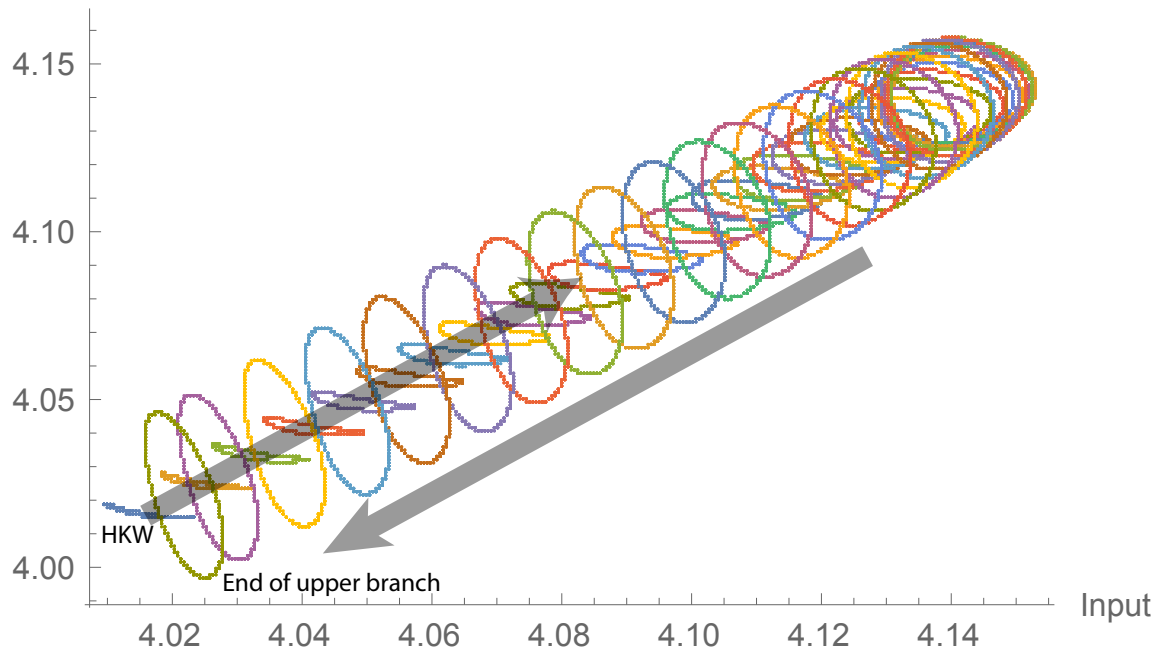


Figure 4.15: Dissipation vs energy input for the upper branch of P8. The HKW solution is the thin blue solution that is continued up to higher dissipation/energy input. However, for finite  $Re$ , there is a maximum velocity gradient that can be maintained, so the energy input is necessarily bounded, and the orbits begin moving down the dissipation/energy input line, eventually becoming the transition branch. While I was hoping to see an especially meaningful change in the orbit topology, there doesn't seem to be a great deal of change in its general structure during any bifurcation.

of the turning points. We can also easily calculate the circumference of each orbit by summing the distance between each individual point over the orbit, and obtain Figure 4.20, which is suggestively similar to Figure 4.6.

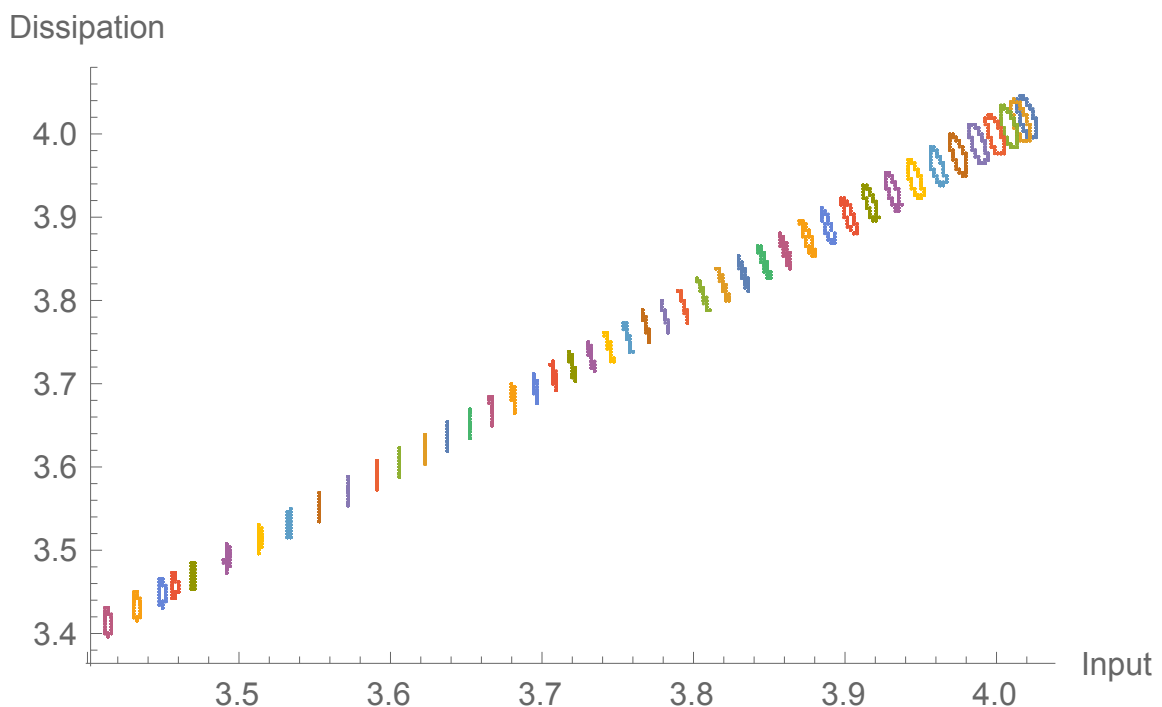


Figure 4.16: The transition branch continues to move down the dissipation/energy input line. As it does so, its area contracts to a near point, and expands again, at which point it becomes the lower branch.

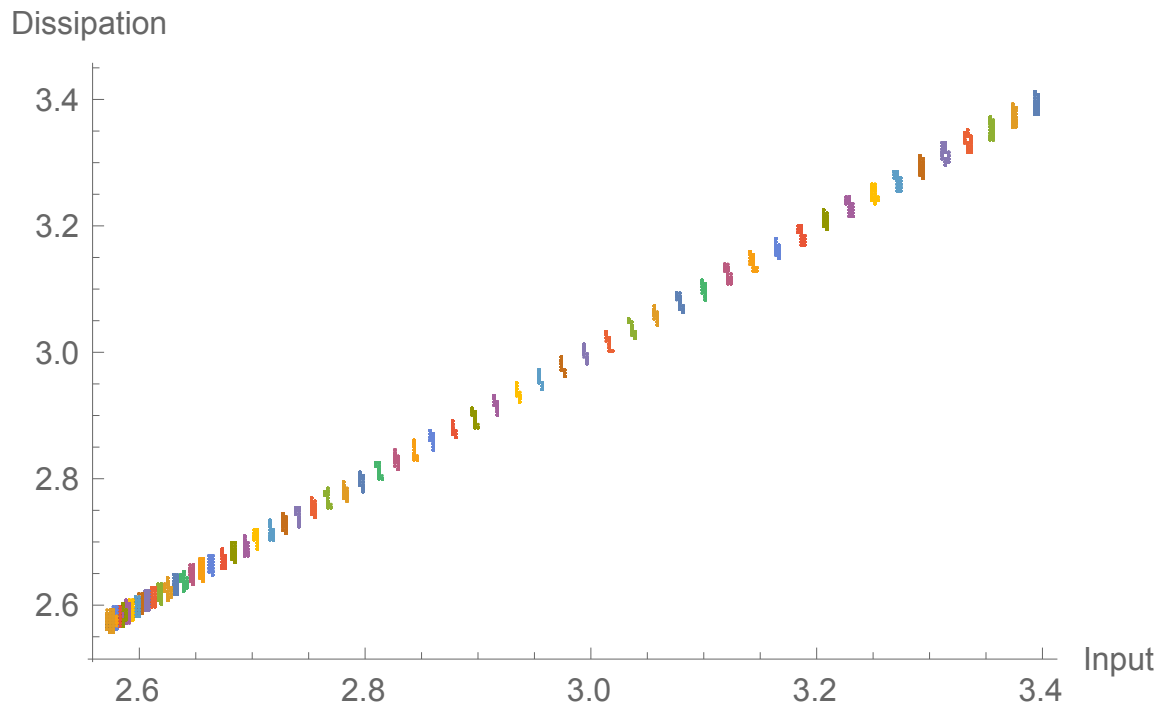


Figure 4.17: The lower branch is even less eventful than the transition branch, and generally maintains its structure through its descent towards the origin of the dissipation/energy input plane. Eventually, it reaches the point where Algorithm 5 fails, and the continuation process halts.

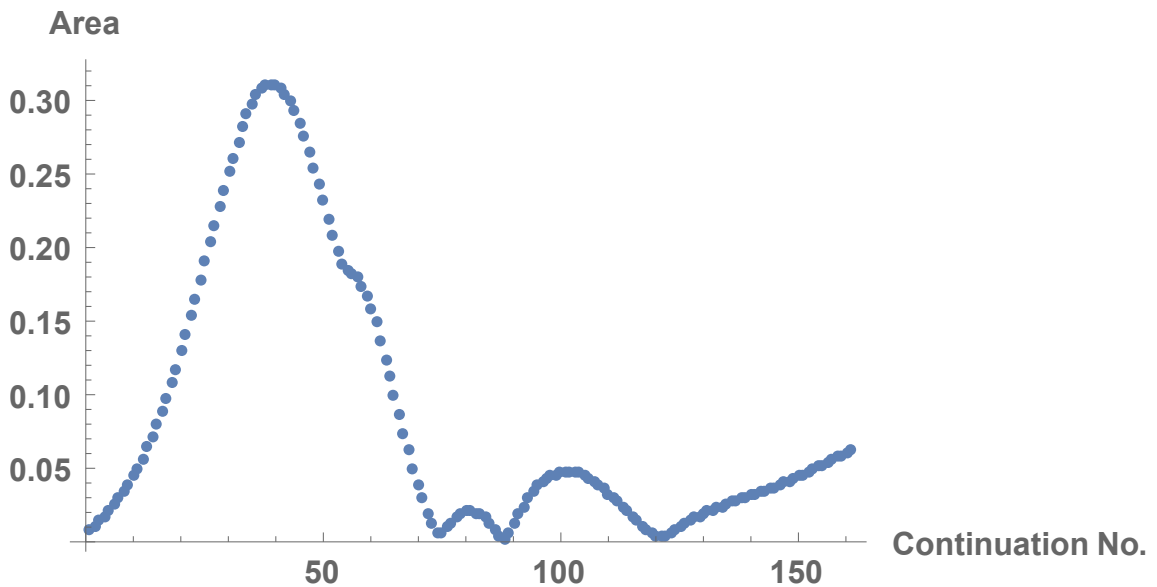


Figure 4.18: Approximate area of P8 at various  $L_z$ . Here, the orbits are ordered by traversing Figure 4.6, beginning from the start of the upper branch. The area function begins looking very smooth and Gaussian, but acquires a kink on its way down, after which it behaves in a more complex manner. The fact that the area in the dissipation/energy input plan goes very low is interesting, but probably not indicative of any behavior that has a global effect.

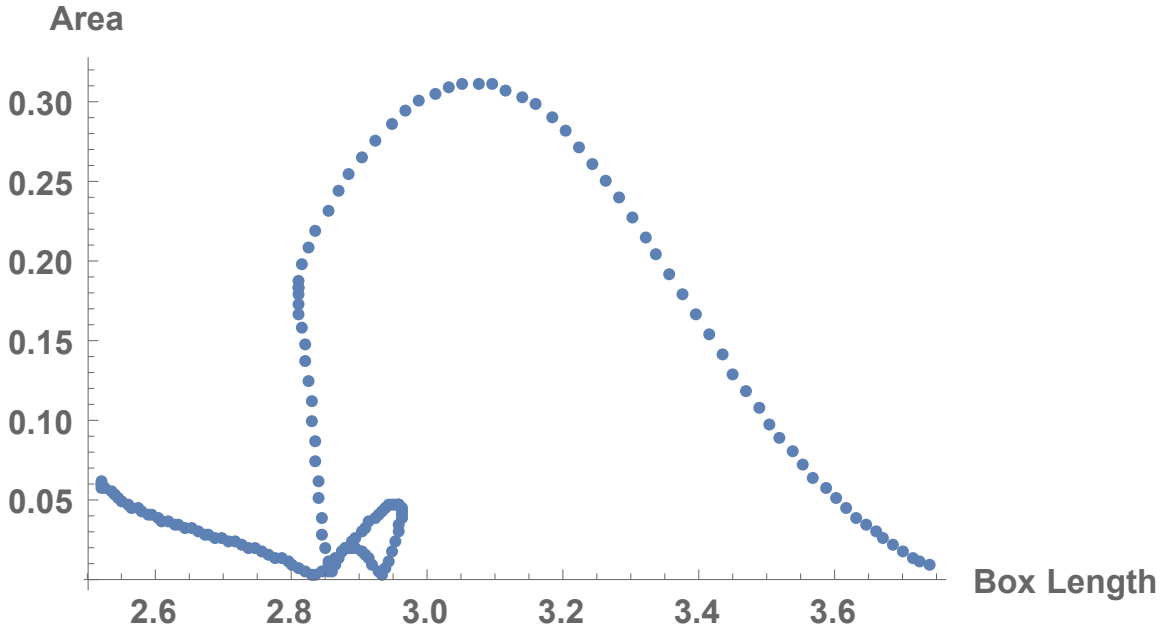


Figure 4.19: When the approximate area of P8 is ordered by  $L_z$ , the features observed in Figure 4.18 take on more meaning. The kink observed in the downwards slope of the Gaussian coincides almost perfectly with the first turning point of Figure 4.6, and the third peak corresponds to the second turning point. While not conclusive, this does show that the turning points are associated with (admittedly slight) structural changes in a physically important projection.

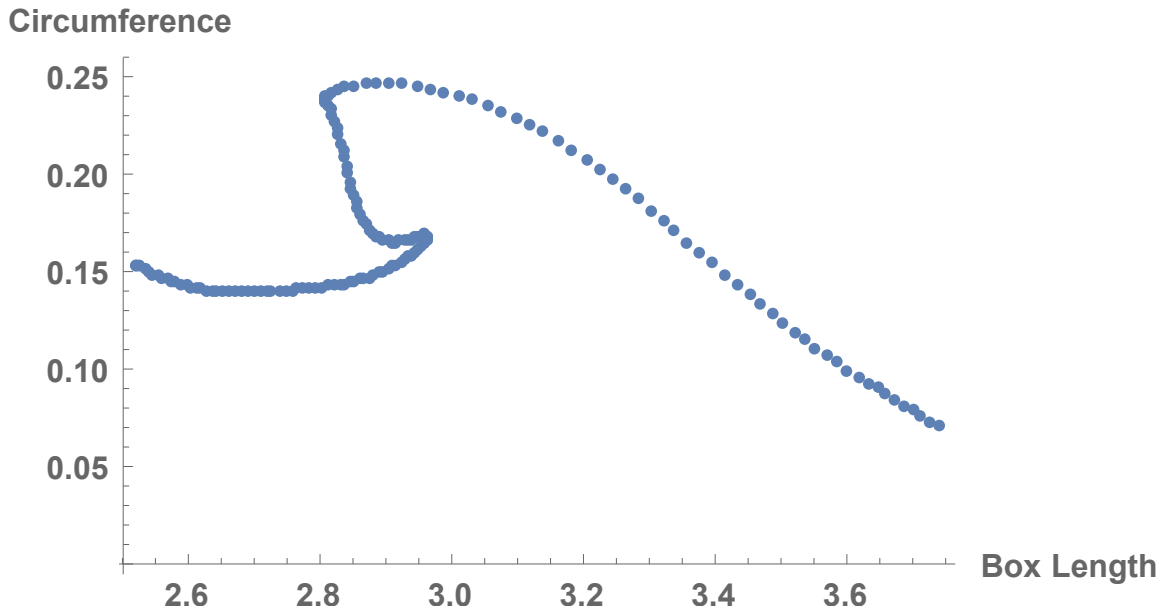


Figure 4.20: The circumference of P8 as a function of  $L_z$ . The similarly to Figure 4.6 is noticeable, and is not as trivial as it may sound - the velocity on a trajectory is not certain *a priori*, so a periodic orbit with a small circumference can still have a long period.

This ends the analysis of the Gang of Four, and of P8 in particular (Though not for lack of material to analyze...). I will now conclude this thesis by giving a quick summary of the key points, discussing the results, and suggesting potential areas of future research.



# Conclusion

Well-chosen, non-frivolous  
epigraphs can enhance a thesis.

---

Michael Scott



# References

- [1] K.-S. Choi, “Fluid dynamics: The rough with the smooth,” *Nature*, vol. 440, no. 7085, pp. 754–754, 2006.
- [2] P. Grassberger and I. Procaccia, “Measuring the strangeness of strange attractors,” in *The Theory of Chaotic Attractors*, pp. 170–189, Springer, 2004.
- [3] D. Borrero-Echeverry, *Subcritical Transition to Turbulence in Taylor-Couette Flow*. PhD thesis, Department of Physics, Georgia Institute of Technology, Atlanta, GA 30332, 2014.
- [4] M. Nagata, “Three-dimensional finite-amplitude solutions in plane Couette flow: Bifurcation from infinity,” *Journal of Fluid Mechanics*, vol. 217, pp. 519–527, 1990.
- [5] J. J. Halcrow, *Charting the State Space of Plane Couette Flow: Equilibria, Relative equilibria, and Heteroclinic Connections*. PhD thesis, Department of Physics, Georgia Institute of Technology, Atlanta, GA 30332, 2008.
- [6] F. Daviaud, J. Hegseth, and P. Bergé, “Subcritical transition to turbulence in plane Couette flow,” *Physical Review Letters*, vol. 69, pp. 2511–2514, 1992.
- [7] S. Pope, *Turbulent Flows*. Cambridge University Press, 2000.
- [8] E. Hopf, “A mathematical example displaying features of turbulence,” *Communications on Pure and Applied Mathematics*, vol. 1, no. 4, pp. 303–322, 1948.
- [9] C. Foias, G. R. Sell, and R. Temam, “Inertial manifolds for nonlinear evolutionary equations,” *Journal of Differential Equations*, vol. 73, no. 2, pp. 309–353, 1988.
- [10] E. N. Lorenz, “Deterministic nonperiodic flow,” *Journal of the Atmospheric Sciences*, vol. 20, no. 2, pp. 130–141, 1963.
- [11] N. Aubry, P. Holmes, J. L. Lumley, and E. Stone, “The dynamics of coherent structures in the wall region of a turbulent boundary layer,” *Journal of Fluid Mechanics*, vol. 192, pp. 115–173, 7 1988.

- [12] O. Dauchot and N. Vioujard, “Phase space analysis of a dynamical model for the subcritical transition to turbulence in plane Couette flow,” *The European Physical Journal B-Condensed Matter and Complex Systems*, vol. 14, no. 2, pp. 377–381, 2000.
- [13] F. Waleffe, “Exact coherent structures in channel flow,” *Journal of Fluid Mechanics*, vol. 435, pp. 93–102, 5 2001.
- [14] G. Kawahara and S. Kida, “Periodic motion embedded in plane Couette turbulence: Regeneration cycle and burst,” *Journal of Fluid Mechanics*, vol. 449, pp. 291–300, 2001.
- [15] D. Viswanath, “Recurrent motions within plane Couette turbulence,” *Journal of Fluid Mechanics*, vol. 580, pp. 339–358, 2007.
- [16] B. Hof, C. W. H. van Doorne, J. Westerweel, F. T. M. Nieuwstadt, H. Faisst, B. Eckhardt, H. Wedin, R. R. Kerswell, and F. Waleffe, “Experimental Observation of Nonlinear Traveling Waves in Turbulent Pipe Flow,” *Science*, vol. 305, no. 5690, pp. 1594–1598, 2004.
- [17] A. De Lozar, F. Mellibovsky, M. Avila, and B. Hof, “Edge State in Pipe Flow Experiments,” *Physical Review Letters*, vol. 108, no. 21, p. 214502, 2012.
- [18] J. F. Gibson, J. Halcrow, and P. Cvitanović, “Visualizing the geometry of state space in plane Couette flow,” *Journal of Fluid Mechanics*, vol. 611, pp. 107–130, 2008.
- [19] J. F. Gibson, “Channelflow: A spectral Navier-Stokes simulator in C++,” tech. rep., U. New Hampshire, 2014. [Channelflow.org](http://Channelflow.org).
- [20] R. Granger, *Fluid Mechanics*. Dover Books on Physics Series, Dover Publications, 1995.
- [21] S. L. Fischer and S. P. Fischer, “Mean corpuscular volume,” *Archives of Internal Medicine*, vol. 143, no. 2, pp. 282–283, 1983.
- [22] C. Clarke and B. Carswell, *Principles of Astrophysical Fluid Dynamics*. Cambridge University Press, 2007.
- [23] R. C. Dorf, *Sensors, Nanoscience, Biomedical Engineering, and Instruments: Sensors Nanoscience Biomedical Engineering*. CRC Press, 2006.
- [24] J. Rotman, *An Introduction to the Theory of Groups*. Graduate Texts in Mathematics, Springer, 1995.
- [25] J. F. Gibson, J. Halcrow, and P. Cvitanovic, “Equilibrium and travelling-wave solutions of plane Couette flow,” *Journal of Fluid Mechanics*, vol. 638, pp. 243–266, 2009.

- [26] U. Frisch, *Turbulence: The Legacy of A.N. Kolmogorov*. Cambridge University Press, 1995.
- [27] R. Peyret, *Spectral Methods for Incompressible Viscous Flow*, vol. 148. Springer Science & Business Media, 2002.
- [28] M. Frigo and S. G. Johnson, “FFTW: An adaptive software architecture for the FFT,” in *Acoustics, Speech and Signal Processing, 1998. Proceedings of the 1998 IEEE International Conference on*, vol. 3, pp. 1381–1384, IEEE, 1998.
- [29] U. M. Ascher, S. J. Ruuth, and B. T. Wetton, “Implicit-explicit methods for time-dependent partial differential equations,” *SIAM Journal on Numerical Analysis*, vol. 32, no. 3, pp. 797–823, 1995.
- [30] W. H. Press, *Numerical Recipes 3rd edition: The Art of Scientific Computing*. Cambridge University Press, 2007.
- [31] R. S. Dembo, S. C. Eisenstat, and T. Steihaug, “Inexact Newton methods,” *SIAM Journal on Numerical analysis*, vol. 19, no. 2, pp. 400–408, 1982.
- [32] Y. Saad and M. H. Schultz, “GMRES: A generalized minimal residual algorithm for solving nonsymmetric linear systems,” *SIAM Journal on Scientific and Statistical Computing*, vol. 7, no. 3, pp. 856–869, 1986.
- [33] W. E. Arnoldi, “The Principle of Minimized Iterations in the Solution of the Matrix Eigenvalue Problem,” *Quarterly of Applied Mathematics*, vol. 9, no. 1, pp. 17–29, 1951.
- [34] I. C. Ipsen and C. D. Meyer, “The idea behind Krylov methods,” *American Mathematical Monthly*, pp. 889–899, 1998.
- [35] L. N. Trefethen and D. Bau III, *Numerical Linear Algebra*, vol. 50. SIAM, 1997.
- [36] J. M. Hamilton, J. Kim, and F. Waleffe, “Regeneration mechanisms of near-wall turbulence structures,” *Journal of Fluid Mechanics*, vol. 287, pp. 317–348, 1995.
- [37] B. Hof, A. de Lozar, D. J. Kuik, and J. Westerweel, “Repeller or attractor? Selecting the dynamical model for the onset of turbulence in pipe flow,” *Physical Review Letters*, vol. 101, p. 214501, 2008.
- [38] S. Taneda, “Experimental investigation of the wake behind a sphere at low reynolds numbers,” *Journal of the Physical Society of Japan*, vol. 11, no. 10, pp. 1104–1108, 1956.